12-2019

Estimation of the Fatigue Life of Additively Manufactured Metallic Components Using Modified Strain Life Parameters Based on Surface Roughness

Peter Grohs
Western Michigan University

ESTIMATION OF THE FATIGUE LIFE OF ADDITIVELY MANUFACTURED METALLIC COMPONENTS USING MODIFIED STRAIN LIFE PARAMETERS BASED ON SURFACE ROUGHNESS

by

Peter Grohs

A thesis submitted to the Graduate College
in partial fulfillment of the requirements for the degree
Master of Science in Engineering (Mechanical)
Mechanical and Aerospace Engineering
Western Michigan University
December 2019

Thesis Committee:

Jinseok Kim, Ph.D, Chair
Muralidhar Ghantasala, Ph.D
Daniel Kujawski, Ph.D

ACKNOWLEDGMENTS

Thanks first to Dr. Kim, who took a chance on me as an undergraduate student and supported me as I balanced school and work, and to my committee, Drs. Ghantasala and Kujawski, for their time, consideration, and willingness to support my research. Thanks also to the financial support of Western Michigan University through the research start-up fund, the Graduate Student Research and Travel Grants, and Engineering College's Graduate Student Travel Grant, without which this research could not have been completed. And finally, thanks to my family, and my wonderful wife, who lovingly tolerated a foolish new husband who decided that crunch time for a thesis was the perfect time to get married. I love you Savannah.

Peter Grohs

ESTIMATION OF THE FATIGUE LIFE OF ADDITIVELY MANUFACTURED METALLIC COMPONENTS USING MODIFIED STRAIN LIFE PARAMETERS BASED ON SURFACE ROUGHNESS

Peter Grohs, M.S.E.

Western Michigan University, 2019

In this study, a method is developed to estimate the effects of surface roughness on the fatigue life of additively manufactured titanium Ti6Al4V, aluminum 7075–T6, and steel 4340 alloys through modified strain life parameters using finite element analysis (FEA). This method is highly beneficial to the fatigue analysis of as-built additively manufactured metal components, which possess rough surfaces that reduce fatigue life significantly but are challenging to analyze directly using finite element simulation because of complex geometries, i.e., modeling an exact surface profile is arduous.

An effective stress concentration factor, incorporating roughness data, is defined to quantify their effects on effective stress and fatigue life. Notched finite element models with effective stress concentration factor values ranging from 3.058 – 10.75, representing rough surfaces from as-built additively manufactured components, are analyzed, and the S–N curves obtained. A parametric study is done to reproduce these S–N curves by using a smooth finite element model with modified strain life parameters. A mathematical model describing the variation of stress concentration in fatigue is incorporated into these lines of constant stress concentration factors to produce a more realistic fatigue model. Finally, there is a relationship established between effective stress concentration factor and modified strain life parameters such that the fatigue life of as-built additively manufactured parts can be easily calculated using finite element simulation by measuring surface roughness data and calculating the new effective strain life parameters, without using an actual rough surface in FEA.

Contents

List of Tables

List of Figures

NOMENCLATURE

R_a	Arithmetic surface mean roughness
R_t	Maximum profile height across domain
R_z	Maximum profile height
$R_{z,ISO}$	Ten point height roughness
$\bar{\rho}_{10}$	10 point valley radii
N_f	Number of cycles to failure
σ'_f	Fatigue strength coefficient
b	Fatigue strength exponent (Basquin's exponent)
ε'_f	Fatigue ductility coefficient
c	Fatigue ductility exponent
K'	Cyclic strength coefficient (H' in some texts)
n'	Cyclic strain hardening exponent
ε	Local (total) strain
σ	Local stress
e	Nominal elastic strain
S	Nominal elastic stress
k_t	Stress concentration factor
k_f	Fatigue stress concentration factor
$\bar{k}_t$	Effective stress concentration factor
$k_{f,real}$	Realistic fatigue stress concentration factor, accounting for variations from loading
q	Notch sensitivity
E	Elastic (Young's) modulus
R	Fatigue load ratio
ν	Poisson ratio
ρ	Density
$\sigma'^{*}_f / \varepsilon'^{*}_f$	Strain life parameters, from parametric analysis
$\sigma'^{i}_f / \varepsilon'^{i}_f$	Strain life parameters, initial, using σ'_f and ε'_f as coefficients
δ	Modified strain life correction factor
$\sigma'^{\delta}_f / \varepsilon'^{\delta}_f$	Strain life parameters, correction factor
$\bar{\sigma}'_f / \bar{\varepsilon}'_f$	Effective strain life parameters for roughness analysis

1 Introduction

Additive manufacturing, or 3D printing, is a method of manufacturing that has a surge in popularity in recent years, particularly in the aerospace industry [1, 2]. In contrast to conventional manufacturing—in which a material solid is shaped into a final geometry using various cutting heads—the additive manufacturing (AM) process produces part geometries by fusing a series of flat layers from a material filament or powder substrate using a computer-controlled deposition head [1, 3, 4]. This method allows complex geometric features to be produced, like internal cooling passages, which are otherwise too difficult for conventional machining [2]. Both metal and polymer parts can be produced using AM, though metallic parts are more challenging to produce due to their higher melting points [1]. Three groups broadly classify AM methods. Extrusion systems force a filament through a heated deposition head. Powder feed systems accelerate powder through a deposition head and fuse it to a build surface using a laser. Powder bed systems use a flat bed of powder, which is selectively fused using a laser [1].

Static properties for conventional metals and AM metals are broadly similar, with differences caused by imperfections in the additive manufacturing process. 3D printed parts primarily differ from conventional materials in fatigue performance. AM parts experience significantly shorter fatigue life and lower fatigue strength than those made from conventional metals. In general, as-built 3D printed metals will experience fatigue failure approximately 50% faster than conventional metals [5, 6]. With AM, unmelted regions of material substrate (pores) or gas pockets (voids) can be present, affecting the overall porosity [7]. The occurrence of these imperfections on the surface of the part form significant stress concentration factors. Pores and voids present on the surface and interior of a part contribute to significant surface roughness, or inhomogeneities on a material's surface. 3D printed parts have surface roughnesses orders of magnitude larger than conventionally machined parts. Surface effects are the primary failure mechanism for 3D printed parts undergoing fatigue loading [5, 7].

The 3D printing processes produce parts that have highly random surface profiles at the microscopic level, which contributes to a characteristically poor fatigue performance and makes accurate representation difficult in finite element analysis (FEA). The real complex surface profile of the final printed part, caused by imperfections and roughness, is highly random and distinct from the ideal CAD geometry used to print the part. The CAD geometry will not accurately represent the as-built 3D printed part for this reason. Several techniques have been developed to represent a real surface algorithmically or import data from actual surfaces into FEA, but this adds considerable complexity to the meshing model. Any intricate geometric feature necessitates adding more elements in the model, which leads to more overall solving time [8–10].

A method to simulate a rough surface using modified material properties rather than a realistic geometry with unmodified material properties has several benefits for FEA. The original CAD drawing of the part can be imported into the FEA software as is, without modification or consideration to the manufacturing method. However, roughness and surface profile data are complex data that are difficult to quantify into a simple parameter. There exists one method that encapsulates four roughness parameters into a single effective stress concentration factor [11]. This method may link roughness to standard fatigue analysis, making fatigue life prediction of as-built 3D printed parts more straightforward. The only input parameters are measurable roughness values from a sample part. However, this linking will require the development of a new method.

1.1 3D Printing Methods

Additive manufacturing has a broad definition, and several manufacturing methods exist. This section outlines their essential functions so that the characteristics of 3D printed parts can be more easily understood.

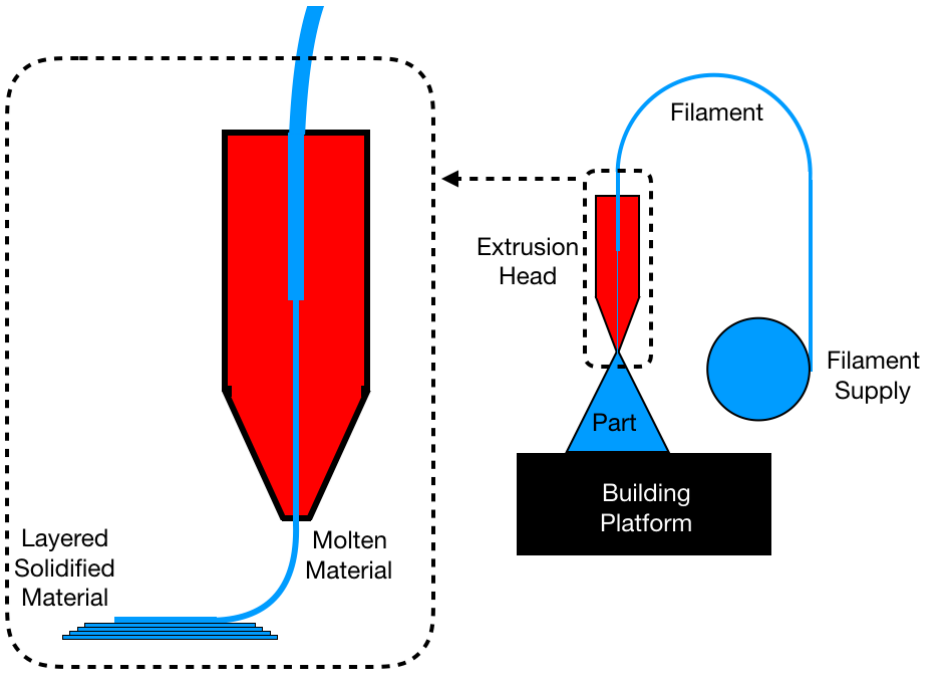

Figure 1: Principles of fused deposition modeling (FDM) extrusion system [12].

The most common method of 3D printing is an extrusion system, also called wire feed systems. This category encompasses some of the simplest and least expensive machines for AM, including most hobbyist machines. In an extrusion system, feed stock in the form of a filament or pellets is heated to just above the melting point and extruded through a computer positioned nozzle. The material rapidly solidifies upon leaving the extruder forming a bead of material at the location of the nozzle. Layers are built up through repeated passes, forming the final part [1]. Figure 1 illustrates this process, showing the feed stock filament, the position controlled extrusion head, and the process for building the part in layers. The final unfinished part features a distinct crisscross, stair-stepping pattern of fused bead in layers, which become more homogeneous as the quality of the machine rises. The most cited method extrusion system is fused deposition modeling (FDM, Figure 1), a filament-based technology, which is a high volume manufacturing technique best suited for plastics. It has relatively poor surface quality, porosity, and accuracy, and requires extensive machining to produce a smooth surface [1, 3]. The filament diameter dictates the layer thickness and is relatively thick for AM. The highly rough surfaces from FDM make it an unsuitable method for many practical

engineering applications. These machines are simple and often used for geometric prototyping using low-cost plastics and rarely metals [3].

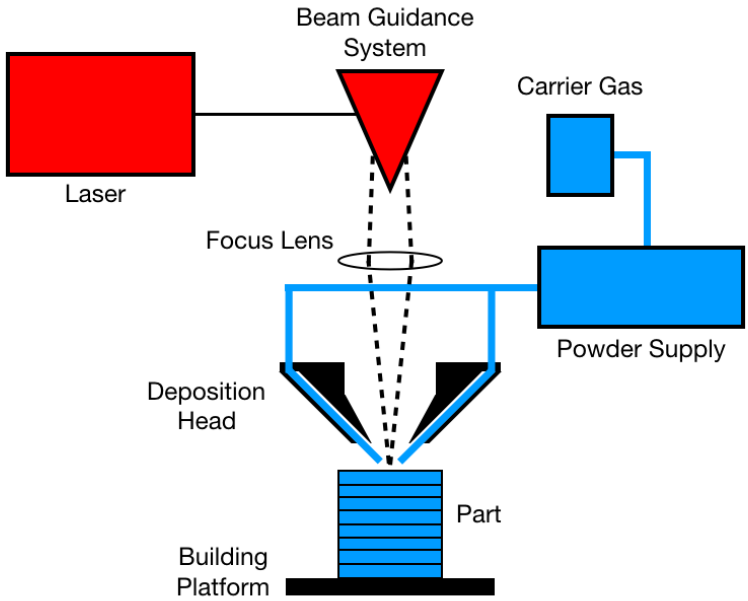

Figure 2: Principles of laser engineered net shaping (LENS) powder feed system [1].

Powder feed systems operate similarly to extrusion systems. They send a stream of powder through a deposition head, accelerated by compressed gas or gravity and heated by a laser, to deposit layers of material on a substrate, building a part up layer by layer. Figure 2 shows a conceptual powder feed system. The beam guidance system and focus lens guides the laser to heat the part surface into a small pool, while the carrier gas expels the powder supply into this pooled part surface. This method can be used to build new parts or, uniquely, to repair preexisting damaged parts [1]. The predominant AM powder feed method is laser engineered net shaping (LENS). With LENS, a laser melts a small region on the substrate surface, forming a pool, consuming the deposited powder, and increasing its size. An advantage of the LENS system is that parts can be several meters in size. However, the accuracy and surface roughness are worse than with other non-extrusion systems [3]. LENS systems often use metals, with the titanium alloy Ti6Al4V being the focus of much research [4, 13–16].

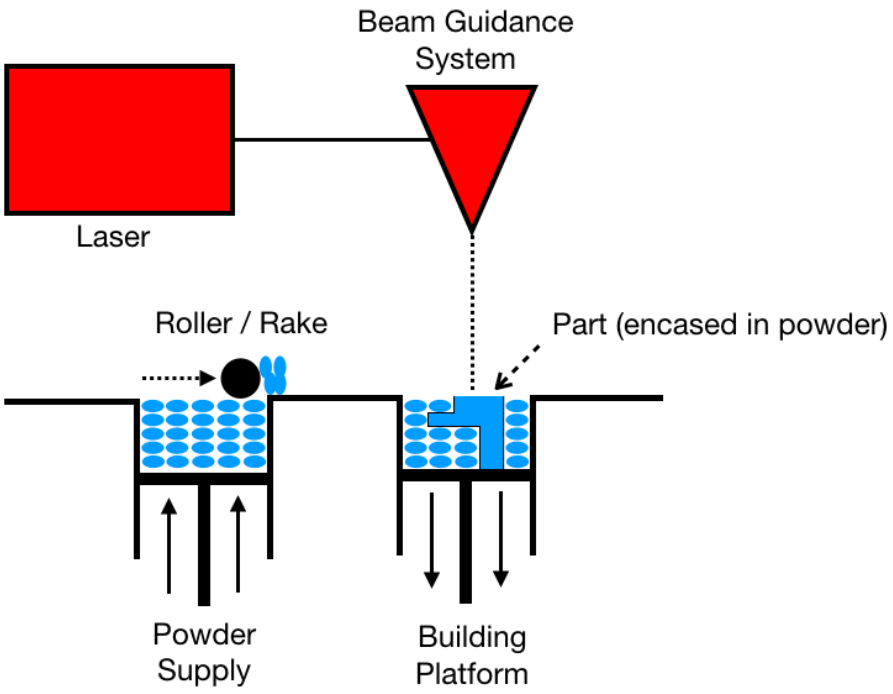

Figure 3: Principles of powder bed AM systems [1].

Powder bed manufacturing differs in principle to extrusion or powder feed systems. It is a selective fusing process rather than a deposition process. In this method, the machine rakes a level layer of material powder onto a work surface. A laser or other focused energy source targets the flat powder and selectively fuses it into thin solid layers. Once the layer is complete, the machine lowers the work surface, it rakes a new layer of powder over the fused surface, and the process repeats. Unused powder encases a finished part within the work area when completed. This powder is blasted off and recycled [3, 16]. Figure 3 illustrates this process. The powder supply platform raises to produce more powder to supply the roller, which pushes powder to the building to building platform, which lowers. The beam guidance system solidifies this new layer of powder.

Two primary systems for powder bed manufacturing exist which use different energy sources to melt the powder: selective laser melting (SLM), selective laser sintering (SLS), and direct metal laser sintering (DMLS) use lasers as their power source, and electron beam manufacturing (EBM) uses a high voltage electron beam [3].

SLM and SLS are very similar processes, with the primary difference being the lower-powered 200 W laser in SLS and the more powerful 400 W laser used in SLM, with the higher-powered laser producing a more homogeneous structure. These processes use both plastics and metals. Both heat the powder to a point just below its melting point before fusing. As its name implies, SLS sinters the powder together into a solid mass. SLS is highly accurate and has good surface quality, but the sintering process leads to reduced homogeneity, which may develop cracks [3]. SLM's higher power laser is enough to completely melt the powder into a part leading to greater homogeneity. DMLS is a trademarked process by EOS Electro Optical Systems and is very similar to SLM and SLS, but restricted to metals only [3]. SLM is the method of most significant interest to current research in laser-based additive manufacturing due to its higher fatigue performance without post-manufacture treatments [4, 17–25].

EBM is a newer technique that is functionally identical to SLM/SLS processes but uses a 30–60 kV electron beam to fuse the powder. Unlike laser-based systems, the build chamber for EBM is under a high vacuum to avoid material oxidation. It is suited for metal parts only and has a lower surface quality than SLM/SLS but a higher output [3]. It tends to have inferior fatigue limits to DMLS and related processes due to more severe surface roughness [26].

1.2 Part Characteristics

Any part produced using additive manufacturing will differ from a conventional machined part in several ways, although static properties, such as ultimate strength or Young's modulus, are similar to conventionally fabricated parts due to fine microstructures [5]. The localized fusion of the 3D printing process is a cause for density variance in 3D printed parts not typically present in wrought materials. These occur in the forms of flaws (pores), in the form of voids and inclusions [14]. These terms are loosely defined and are highly dependent on the method of manufacture. Voids are typically caused by bubbles of

trapped gasses present during manufacturing or by lack of fusion pockets of unfused powders. In one study, the average diameter of gas pore voids in a sample of EBM Ti6Al4V was less than 10 μm, with spherical pore diameters upwards of 50 μm. SLM parts have fewer significant gas pore voids, with the largest size of lack of fusion pores being 240 μm for SLM and 320 μm for EBM [4]. Inclusions occur less commonly than voids and are caused by "contamination", "particle debris", and "un-melted powder". They have a similar effect as voids, though overall part porosity is less affected [14]. A study that simulated the fatigue effects of voids and inclusions with identical diameters using FEA concluded that broadly similar results occurred with either types of flaws [27].

The microscopically random geometry of additive manufactured parts contributes to a characteristically poor fatigue performance. Voids and inclusions function as stress concentrations throughout the part, and, if present at the surface, contribute significantly to local and overall roughness. Surface roughness is caused by both solidification of the melt pool and by partly melted powders for both DMLS and EBM processes [26]. Stress concentrations are locations where crack growth originates, which may occur at any point in the volume of the part. Although it is shown that the location of the flaw, particularly its proximity to the surface, has a much more significant effect on the fatigue life of the part than the pore size. Surface flaws the primary cause of fatigue failure in AM parts [23].

Additionally, steep temperature gradients and rapid thermal cycles in 3D printing produce parts with high residual internal stresses, which can lead to accelerated crack growth. Crack growth originating from part interiors may be mitigated to a certain degree by post-process heat treatments such as hot isostatic pressing (HIP) [3, 17]. Though accurate at the macroscopic level, 3D printed parts are inherently geometrically random at the microscopic level, typically requiring machining or other post-processing treatments for precision applications.

1.3 Post-manufacturing Treatments

Post manufacturing treatments can mitigate undesirable part characteristics like porosity, residual stress, and roughness, and vary on their effectiveness and feasibility. As AM parts have broadly identical static properties to conventional materials, these treatments primarily serve to increase the fatigue properties of the parts [5, 13]. Surface flaws, namely surface level pores, voids, and roughness, have the most significant effect on the fatigue performance of as-built parts. With roughness values such as R_z being upwards of 200 μm, and pores with diameters of approximately 300 μm, polishing can be a highly effective method to increase fatigue life. Polishing produces a smooth surface with negligible roughness values. However, polishing can be impractical or unfeasible for parts with complex shapes and intricate internal geometries.

Shot peening is a well-known method to induce compressive stresses on the surface of a part to suppress crack growth and improve fatigue performance, though in practice it proves ineffective as a treatment to prevent crack growth [20, 28]. One study found that shot peening actually reduced the fatigue limit of an SLM Ti6Al4V part by 15% compared to a polished sample, concluding that the compressive surface stresses are balanced by tensile stresses in the part's interior, to detrimental effect [21].

Hot isostatic pressing (HIP) is a heat treatment used to reduce the effects of pores and inhomogeneity for AM parts. It subjects a part to a high temperature, high pressure, inert gas environment for several hours to reduce the porosity of the part. A typically HIP treatment will subject a part to a 1000°C, 1000 bar argon gas environment for 2–4 hours [18, 19, 29]. HIP is routinely done for many studies in the literature with little mention, particularly for SLM parts [4, 17–25]. It can increase the fracture toughness of SLM parts by 30%, but it does not affect un-machined EBM: the EBM method is performed in a high vacuum, high temperatures environment that is similar to HIP treatments (see section 1.1), causing this heat treatment to be less effective on it [4, 19, 28–30]. HIP heat treatments are effective in reducing internal flaws and removing almost all of a part's internal porosity, eliminating

almost all internal crack growth from within the part. Critically though, HIP treatments do not affect surface pores, which are the primary source of fatigue failure and remain the primary limiting factor for as-built 3D printed metals [5, 13, 14]. A combination of polishing and HIP will produce a 3D printed part with the highest fatigue strength [4, 19]. The fatigue properties of polished/HIP'ed SLM parts are "more comparable" and "similar" to conventional parts [28]. However, HIP can produce larger grain sizes in post-treated parts, which can increase the fatigue crack growth rate [26].

Post manufacturing treatments can improve fatigue performance of AM parts nearly to that of conventional machined parts, but they are often unfeasible, not effective, or impractical for many of AM's most desirable applications. It is advantageous to limit AM research into the area of as-built part development if 3D printing is to further develop as a viable alternative.

1.4 Roughness

The primary engineering limiting factor of 3D printed parts is as-built fatigue performance, with surface effects being the most critical factor to that. Roughness is a general measurement of irregularities present on the surface of a component. Surface roughness can be thought of in the same way as small cracks [31]. There are over a dozen roughness parameters that quantify a specific quality of the surface profile; however, there is no one agreed-upon roughness parameter standard to compare multiple components like-for-like.

Final surface conditions of AM parts are highly dependent on process and geometry; the manufacturing process can introduce innumerable chaotic features, creating a chaotic surface at the microscopic level. In general, primary roughness describes overall surface waviness, and secondary roughness is the presence of partially fused substrate [26]. Figure 4 shows a scanning electron microscope image of two specimens, one produced using DMLS powder bed manufacturing, and the other with EBM powder bed manufacturing, and illustrates these roughnesses and the generally random surface of as-built 3D printed

materials.

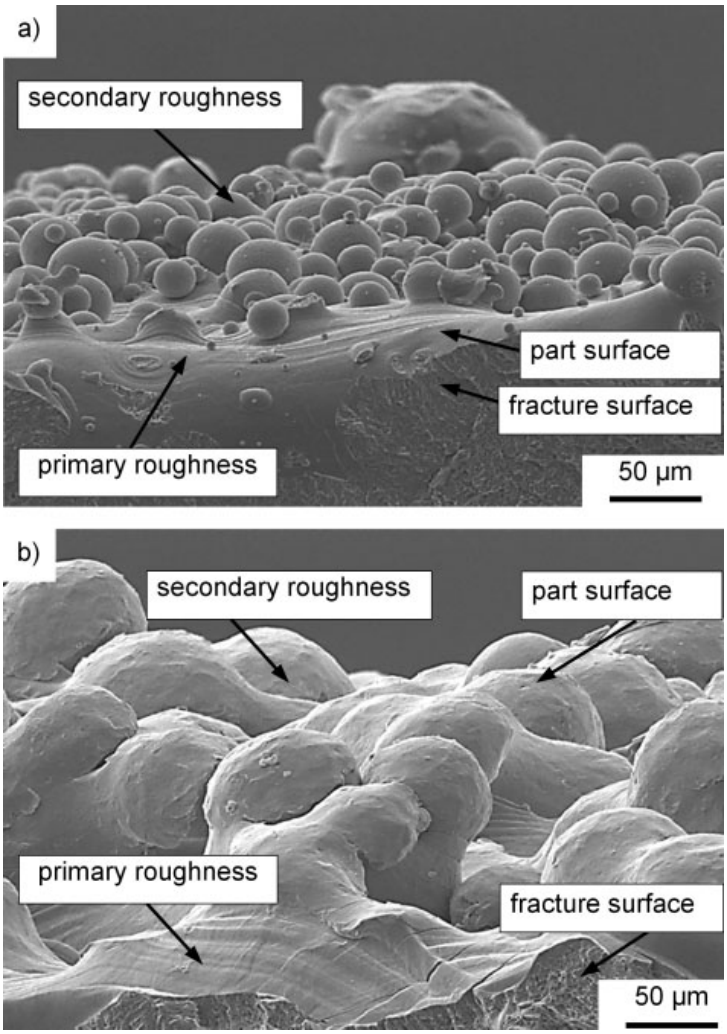

Figure 4: Scanning electron microscope for two specimens produced using (a) DMLS ($R_a = 13$ µm, $R_t = 110$ µm) and (b) EBM 3D printing ($R_a = 27$ µm, $R_t = 214$ µm) [26].

The most commonly reported roughness parameter in literature is mean profile height, R_a, which measures the average true profile height of a sample region compared to the ideal surface height. The ubiquity of R_a as a roughness parameter is mostly historical rather than from merit. R_a does give an overall idea of the total surface variance of a sample region, however.

$$R_a = \frac{1}{l} \int_0^l |Z(x)| \, dx \tag{1}$$

where $Z(x)$ is the depth function of the part surface with respect to the surface axis.

R_z, or maximum profile height, is a more straightforward roughness parameter, defined as the height difference between the peak height, R_{max}, and valley depth, R_{min}, of a surface profile. If the height difference is defined over a portion of the domain, $R_{z,i}$ is more appropriate, as there will be several R_z terms over different sections of the domain. When the domain is large or constitutes the entire surface of a component, total profile length, R_t may be specified.

$$R_z = \left| z_{max,i} - z_{min,i} \right| \tag{2}$$

$$R_t = |z_{max} - z_{min}| \tag{3}$$

where $z_{min,i}$ is the depth of the lowest valley from the ideal surface height, $z_{max,i}$ is the height of the highest peak from the ideal surface height, and z_{min} and z_{max} and the lowest valley and highest peak along the entire domain, respectively. Figure 5 provides a graphic demonstration for how roughness parameters R_a, R_z, R_t, z_{min}, and z_{max} are calculated, to complement equations (1) through (3).

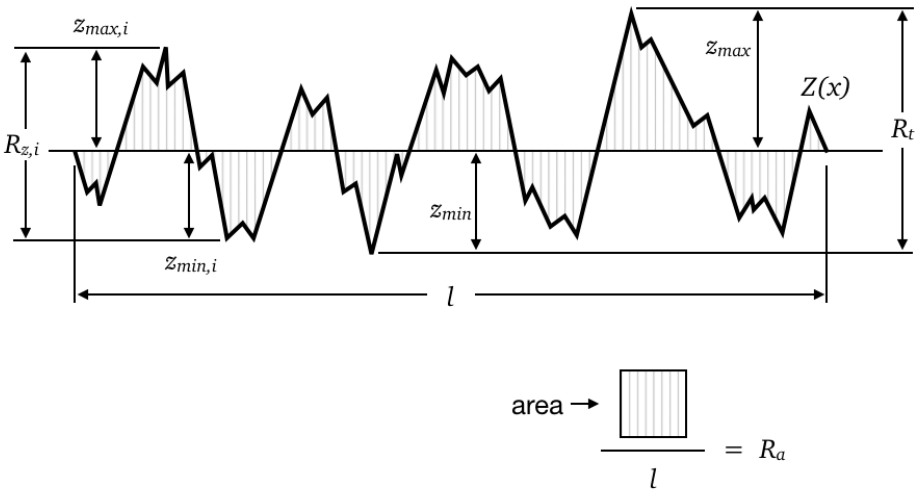

Figure 5: Definition of common roughness parameters.

1.5 Modeling

Computer FEA simulation is an attractive option for verifying the viability of 3D printed designs due to the long manufacturing times required — typically hours even for simple parts a few centimeters high. Unfortunately, the random porosity and surface roughness present in AM parts are challenging to represent directly in FEA. Meshing a full-sized realistic model, as shown in Figure 4, using typical industry and academic computer workstations is unfeasible. Research in modeling realistic as-built geometries using FEA is sparse; studies that incorporate simulation often assume a machined or other ideal surface or will ignore porosity effects. Studies into material properties of 3D printed materials often do no computer modeling at all before testing. Assuming an ideal smooth surface is acceptable for a standard symmetric fatigue testing specimen, which has simple, regular geometry and is easy to polish after printing. However, this assumption is implausible for the sort of irregular geometries often requested of AM manufacturing, where intricate designs make surface refinishing difficult. Because the surface profile of as-built 3D printed parts is the limiting factor to fatigue performance, it is advantageous to simulate a part that represents this quality in FEA.

The most straightforward model of a roughness effect is the regular stair-stepping effects produced by FDM and, to a lesser extent, by the other 3D printing methods. Ahn et al. [32, 33] developed two methods to predict R_a for FDM using filament geometry and deposition angle of the nozzle, which matched the measured data to within 3–5 μm. A related geometric model for FDM achieved 5.7% accuracy to actual results for R_a [34]. Other geometric models for SLM produce similar results [35]. Figure 6 shows a clear demonstration of the filament stair-stepping effect produced by FDM. Each cross-cross layer is one layer produced by the filament.

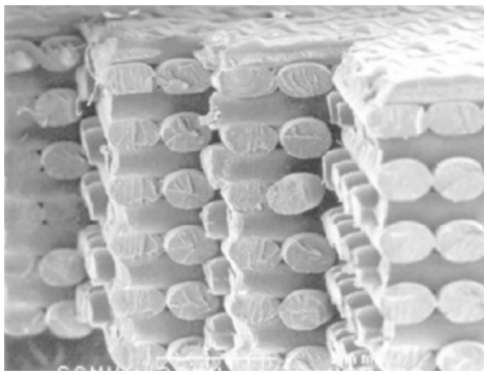

Figure 6: Interior stairstep effect within FDM parts [32].

Statistically generated surfaces are a better way to represent the random surface profile of as-built 3D printed parts. These methods modify an existing FEA mesh using several input parameters. Research done by Thompson documents this procedure using Ansys Mechanical APDL [8]. The first method generates a normal Gaussian distributed rough surface, assuming a regular part with a simple geometry, that was not wavy, and with a constant surface inhomogeneity effect across the surface defined by asperity width, length, and maximum height. Figure 7 shows the Gaussian distribution geometry and mesh used by Ansys. The study compares four mesh algorithms, but standard roughness terms such as R_a and R_z were not incorporated. In a later publication, a similar technique produced anisotropic surfaces with more complex features, such as waviness or irregular shapes, but the study did not go into detail how this is implemented [10].

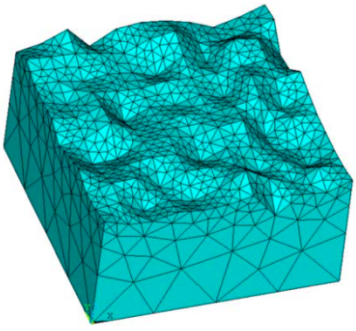

Figure 7: Statistically generated roughness model rough surface using key points, exaggerated 100 times [8].

Beyond generating random roughness values in software, 3D surface profile data measured from as-built parts using optical profilometers could be used to modify a finite element mesh. The primary disadvantage of this is that a sample has to be built before it can be simulated. However, this allows nondestructive simulated testing of the part using an accurate model to the specimen. One study of note captured x, y, z coordinates of a material and used to generate node locations of a mesh in Ansys Mechanical ADPL. The result had good matching with the actual test, despite the model using only 1/3 of the surface data at a resolution of 3 μm to save computation time [9].

All these methods have their limitations. A focus on R_a for many models does not take into account random geometric pores and voids, which form the greatest stress concentrators. These models may be better suited to friction and wear analysis. The Ansys models require significant manipulation to the geometry of a model in FEA, use prodigious meshing, and have understandably long processing times. Additionally, their intended use is for regular, flat geometries, which are unrealistic for practical engineering. Models that incorporate easily measured roughness parameters that do not require any modification to geometry for FEA is an ideal solution.

1.6 Effective Stress Concentration Factor

An alternate method, that utilizes an effective stress concentration factor term, $\bar{k}_t$, which is a function of R_a, R_t, 10-point height roughness $R_{z,ISO}$, and 10-point valley radii $\bar{\rho}_{10}$. ($\bar{k}_t$ is described in detail in section 2.5). The method was initially developed for polymers and has demonstrated good accuracy for as-built 3D printed Ti6Al4V. This method attempts to increase the effective local stress response for use in standard fatigue life analysis. Stress concentrations, like severe roughnesses, will reduce part life [11].

$$\bar{k}_t = 1 + n\left(\frac{R_a}{\bar{\rho}_{10}}\right)\left(\frac{R_t}{R_{z,ISO}}\right) \tag{4}$$

$$n = \begin{cases} 1 & \text{shear} \\ 2 & \text{tension} \end{cases} \tag{5}$$

$$R_{z,IZO} = \frac{1}{5}\left[\sum_{i=1}^{5} z_{i,min} + \sum_{j=1}^{5} z_{j,max}\right] \tag{6}$$

$$\bar{\rho}_{10} = \frac{1}{5}\left[\sum_{i=1}^{5} \rho_{i,min}\right] \tag{7}$$

where $\rho_{i,min}$ are the radii of the deepest valleys measured in a sample. The study finds a good correlation between fatigue life and the effective fatigue stress concentration $\bar{k}_t$, shown in Figure 8. Straight lines indicate predicted response, and points indicate experimental fatigue results using a smooth specimen, a specimen with $R_a = 22.7$ µm ($k_f = 4.21$), and a specimen with $R_a = 31.4$ µm ($k_f = 6.04$). However, this relation is achieved through empirical relations only, with an engineering reference table based on the ultimate strength of the material used with the 3D printed Ti6Al4V, producing an empirical scaler f, which modifies the endurance limit at 10^3 cycles, $\sigma'_{f,10^3}$. The predicted $\bar{k}_t$ scales the run-out stress at 10^7 cycles for a smooth specimen for two different specimens. A straight line on a log–log graph connects $\sigma'_{f,10^3}$ to the run-out stress levels and is plotted with a set of experimental data, shown in Figure 4. This method has good accuracy, but is challenging to implement in FEA as it is currently used — applying a single notch with a known $\bar{k}_t$ at the point of peak stress is difficult for parts models with complex geometries.

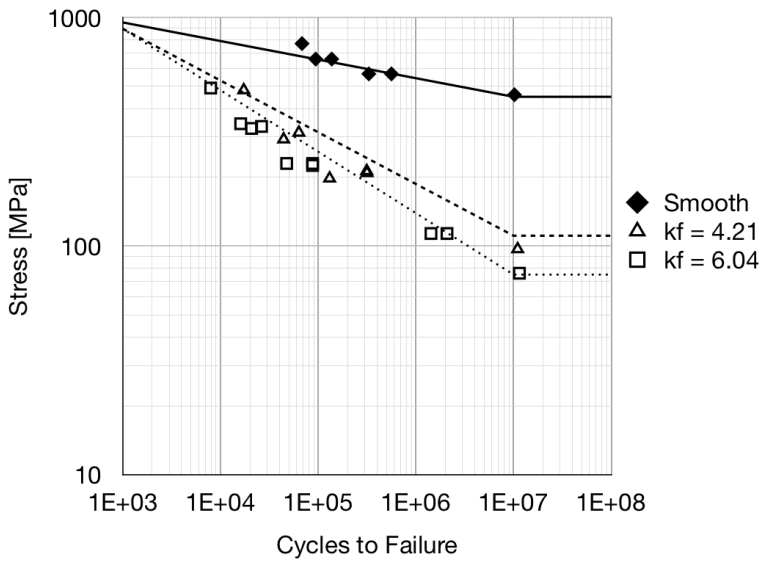

Figure 8: S–N correlation to experiments (points) of as-built Ti6Al4V specimens using $\sigma'_{f,10^3}$ and runout stress, and predicted $\bar{k}_t$ (lines). A smooth specimen, a specimen with $R_a = 22.7$ µm ($k_f = 4.21$), and a specimen with $R_a = 31.4$ µm ($k_f = 6.04$) are shown [11].

1.7 Summary

As described in section 1.5, current models with statistically realistic surface roughnesses fall short in several ways. They use probabilistic algorithms to produce an irregular, random surface that is not customizable to specific roughness parameters such as R_a or R_z, or require 3D profiling of an entire part surface, requiring substantial investment in measurement equipment. Additionally, all the models require significant modifications to the CAD model and a more complex mesh. All this adds time and cost to the simulation. In an ideal case, the FEA simulation of an as-built AM part would not require any modification to the model geometry. FEA would use the same CAD file sent to the AM CAM software without modification.

Given data on part roughness and using the effective stress concentration factor $\bar{k}_t$ described in section 1.6, it may be possible to approximate the effects on as-built 3D printed surface roughness on fatigue life by applying a notch, or, ideally, by selectively modifying material properties such as strain life. The resulting mesh would be much simpler for the

former case, or identical to the original for the latter. In the latter method, a simple profilometer measures an as-built 3D printed specimen for roughness parameters R_a, R_t, $R_{z,ISO}$, and $\bar{\rho}_{10}$. New strain life parameters could then be calculated using a formula and applied to the existing FEA model. The predicted fatigue life for the rough part is calculated using a smooth specimen, with surface effects accounted for in the strain life parameters. This case is the focus of the following research.

2 Background

This section describes additional elements required to perform strain life fatigue analysis using finite element analysis in Ansys Workbench and describes stress concentrators in detail.

2.1 Strain Life Analysis

Stress life and strain life analysis are two fatigue methods available in Ansys Workbench to predict the cyclical life of any part [36]. In general, stress life is suitable only for high cycle fatigue. Additionally, in Ansys, stress life analysis relies on tabulated experimental S–N data from a fully reversed test of the material. For this reason, a parametric study of stress life in Ansys Workbench is difficult or impossible because of the requirement of an S–N curve. It is also less accurate at low cycles.

Conversely, strain life accounts for plasticity during high stress, low cycles fatigue loading, improving results for both low and high cycle fatigue. It is superior to stress life when local plastic behavior is possible, such as the case with notches. Furthermore, the strain life equation uses four material properties: σ'_f, b, ε'_f, and c (see Nomenclature), which, unlike for stress life analysis, can be parametrically varied in Ansys. Due to these benefits, both practical and conceptual, this research uses strain life analysis.

The results of a fully reversed ($R = -1$) strain-controlled fatigue experiment determine strain life parameters σ'_f, b, ε'_f, and c for a material by plotting elastic and plastic strain amplitudes seperately with respect to their reversals to failure, $2N_f$, on a log–log plot. Figure 9 illustrates the procedure. ε'_f is the intercept of the plastic strain amplitude (ε_{pa}) curve at $2N_f = 1$, c is the slope of this curve. σ'_f is determined by the intercept of the elastic strain amplitude curve, and b is the slope of this curve. In the figure, black points are the total strain amplitude for the test and their associated cycles to failure, blue points are the elastic portion of the strain amplitude for that test, and red points are the plastic portion of the strain

amplitude for that test. Together, the blue and red points add up to the black for one test.

$$\frac{\Delta\varepsilon}{2} = \frac{\sigma_f'}{E}(2N_f)^b + \varepsilon_f'(2N_f)^c \tag{8}$$

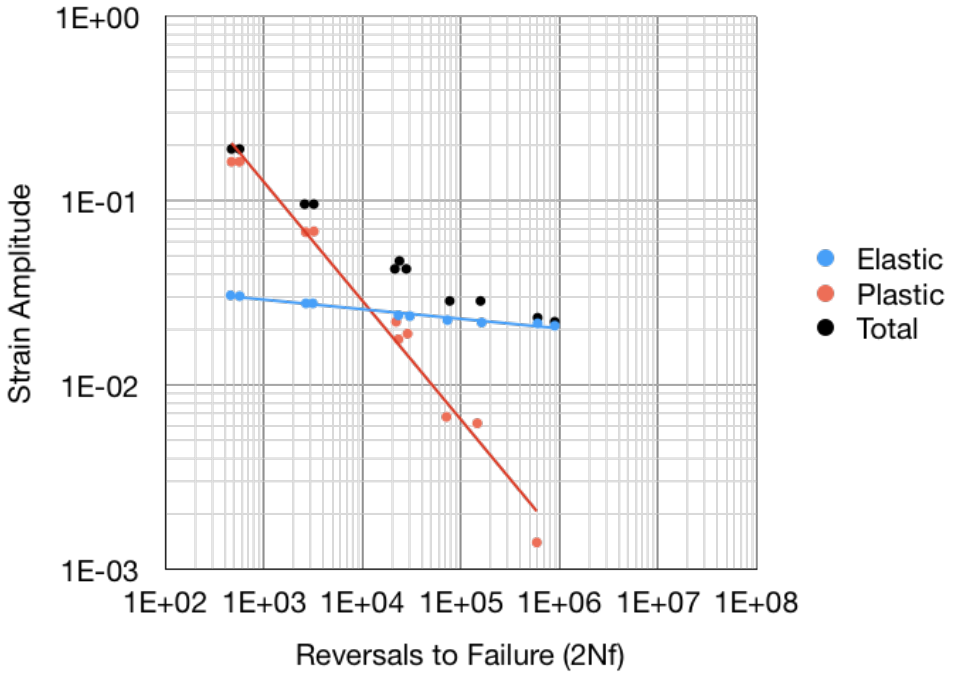

Figure 9: Sample strain life plot, illustrating how to derive strain life parameters σ_f', b, ε_f', and c for RQC-100 steel. Intercepts occur at $2N_f = 1$ for this logarithmic axis [37].

Published data from literature experiments often vary from fully reversed load conditions. A mean stress theory may be applied to account for this. The Morrow and Smith-Watson-Topper (SWT) approaches in equations (9) and (10), respectively, are available in Ansys Mechanical to modify the strain life equation for non-fully reversed loadings. Simulations are done with ideal fully reversed loadings only, so mean stress theories are not utilized.

$$\frac{\Delta\varepsilon}{2} = \frac{\sigma_f' - \sigma_{mean}}{E}(2N_f)^b + \varepsilon_f'(2N_f)^c \tag{9}$$

$$\sigma_{max}\frac{\Delta\varepsilon}{2} = \frac{(\sigma'_f)^2}{E}(2N_f)^{2b} + \sigma'_f\varepsilon'_f(2N_f)^{b+c} \tag{10}$$

2.2 Ansys

The finite element software package used for these simulations is Ansys Workbench. It is highly scriptable for parametric study, allows new materials to be easily defined with units, and has a robust fatigue module. A limitation of Ansys Workbench is the lack of fine meshing controls in the preprocessing. In practice, a user is limited to manipulating the parameters of a limited set of automated meshing algorithms to achieve a quality mesh. 2D analysis is limited to PLANE182 or PLANE183 elements, which are linear or quadratic 2D elements, respectively, with nodal displacement degrees of freedom in x and y directions only [38]. These elements are quadrilateral, but the meshing algorithm may forcibly degenerate them into triangular elements. A user can request to override this behavior, but the meshing engine will automatically overrule this option if the geometry is impossible to reproduce with an all quad mesh. A model is limited to global meshing controls only, with options for precise local refinements being minimal. Therefore, it is necessary to balance refinement for areas of concern and mesh efficiency in noncritical areas when selecting global mesh algorithms and parameters.

Five size function algorithms are available for 2D meshing: Adaptive, which is an all automatic meshing operation with minimal settings; Curvature, which examines part curvature to generate mesh which does not violate a maximum curvature normal angle; Proximity, to specify a minimum number of elements between two edges; and Uniform, which incorporates growth rate and global element size controls only. Proximity and Curvature can be combined. In a comparison between these five algorithms in initial tests, the combined Proximity and Curvature produced the highest quality mesh, which followed the curve of the rough surface accurately and produced regular quadrilateral elements in both the focus area and in areas of least concern for both smooth and notches models. For

areas in the model where steep gradients in the solution are expected, Ansys allows a refinement feature to be added to gradually split elements, making the mesh in that region finer. A maximum refinement, or element division, of 3 is possible, which splits one element into 16 elements for the desired region.

Ansys Workbench incorporates fatigue analysis by utilizing the built in fatigue tool. This tool allows applied loading conditions on the model to be cycled, determining the number of loading cycles to failure to be predicted from either stress or strain analysis, selected as an option by the user. As specified in section 2.1, this research utilizes strain life analysis. Ansys implements the following procedure to predict the number of cycles to failure for a FEA model using strain life.

First, the peak loading condition for the model is applied, and the finite element model is solved for ideal elastic stress, S, using finite element methods. However it is noted that the strain life equation (equation (8)) uses total (elastic + plastic) strain amplitude as input. A number of assumptions are made by Ansys to determine total strain amplitude from ideal elastic stress. It it assumed that the material behavior will be nominally elastic for the given loading condition, therefore an ideal elastic strain, e, response, or $e = S/E$, is calculated. Ansys then links ideal elastic stress and strain to total stress and strain (σ and ε, respectively) with Neuber's rule, equation (11).

$$\varepsilon\sigma = k_t^2 eS \tag{11}$$

Ansys assumes a k_t value of 1 for equation (11), which can be explained as follows. In manual calculations, k_t is applied theoretically in the equation only, with no consideration taken for its actual location. However, given a finite element model with a sufficiently fine mesh, the higher stress at the point of stress concentration will be solved for directly. Because this local stress response around the concentration factor is known, k_t does not need to be incorporated in Neuber's rule. If a notch or other stress concentrator is present in the geometry, it is assumed that the mesh will be fine enough in the stress concentration region

to account for any localized stress behavior.

A second equation is needed to solve equation (11) and determine the total stress and strain response for the entire finite element model. This is achieved using the Ramberg–Osgood equation for cyclic stress-strain response of a material, taken from a plot of the stable half-life hysteresis loop: equation (12). Figure 10 shows these hysteresis loops, or the relationship between stress and strain under cyclic loading, for three different strain controlled experiments, taken at $0.5N_f$. The tips of the three loops are connected by fitting the curve of equation (12), which determines parameters K' and n'.

$$\Delta\varepsilon = \frac{\Delta\sigma}{E} + 2\left(\frac{\Delta\sigma}{2K'}\right)^{1/n'} \tag{12}$$

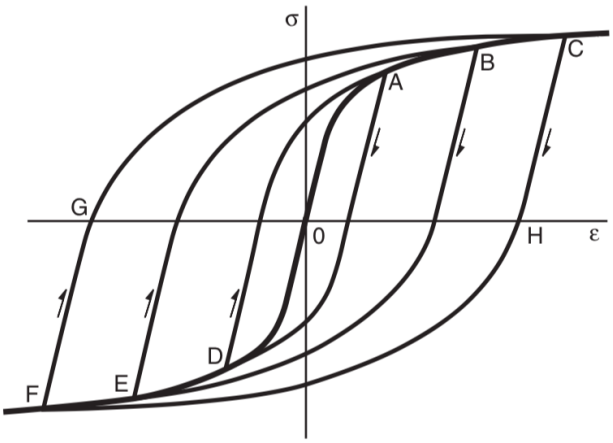

Figure 10: A theoretical hysteresis loop to determine K' and n' (connecting tips 0–A–B–C). Three hysteresis loops are shown (0–A–D, 0–B–E, and 0–C–F), which are produced using strain-controlled fatigue tests to failure at three different strain amplitudes [37].

Equations (8) and (11) are then solved together to determine total stress and strain response. They are solved iteratively, as their relationship is nonlinear. Once total elastic strain, ε, is known for the finite element model, equation (8) can be solved to determine the number of cycles to failure for the model.

2.3 Simulation Geometry

A testing geometry standard is used for consistency with published experiments, although a geometry designed for physical testing is not strictly necessary for finite element analysis. ASTM E466 is a testing standard to obtain fatigue strength of metallic materials subject to constant amplitude uniaxial loads and primarily experiencing elastic strains. The 2015 version of the standard (ASTM E466–15) notes the utility of this standard for stress controlled experiments to "determine the effect of variations in material, geometry, surface condition, stress, and so forth, on the fatigue resistance of metallic materials subjected to direct stress for relatively large numbers of cycles." [39] This standard is often used by published studies to test the fatigue performance of 3D printed parts [6, 17, 20, 24, 28]. The standard describes geometry requirements for straight necks, continuous radius necks, and loading conditions for a valid test. Figure 11 is taken from this standard, and shows an axisymmetric geometry specified in the standard. This model is used as the basis for the finite element analysis models. Table 1 lists geometric parameters for Figure 11, which abide by the standard. They are used to define the FEA model.

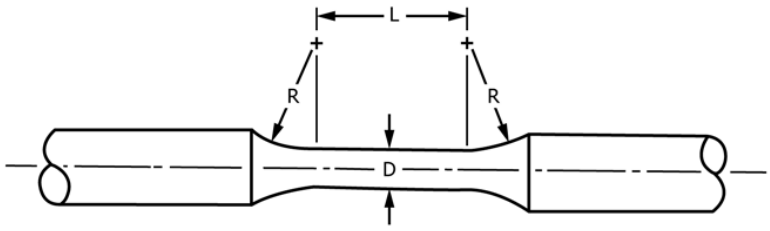

Figure 11: Axisymmetric model for uniaxial testing as defined in ASTM E466–15, used for simulations [39].

Table 1: Geometry parameters for FEA models which abide ASTM E466–15 standard for uniaxial axisymmetric fatigue testing.

D	5mm
L	10mm
R	50mm
D_{shank}	12mm
L_{total}	70mm

2.4 Notches

Notches produce stress concentrations at their root in a way that is calculated analytically. A study examining stress concentration geometries describes the stress concentration factor of a circular notch as a function of its root depth h, the angle of its walls θ, and the radius of the notch root ρ. Figures 12 and 13 show a graphic representation of this geometry and how stress concentration k_t is defined based on the geometric relations. A minimum stress concentration factor of ≈ 3 is possible because the roots of all the notches are circular, meaning a notch with a circular profile can multiply the stress at its root by a minimum factor of three [40].

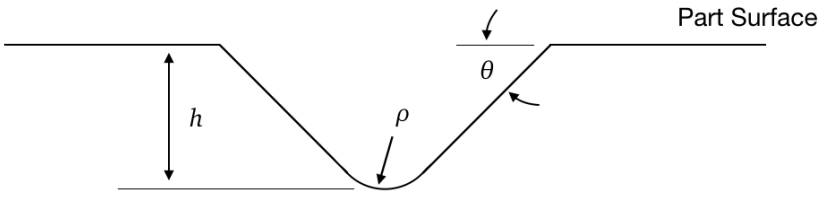

Figure 12: Geometry of Circular Notches defining notch depth h, notch radius ρ, and notch angle θ [40].

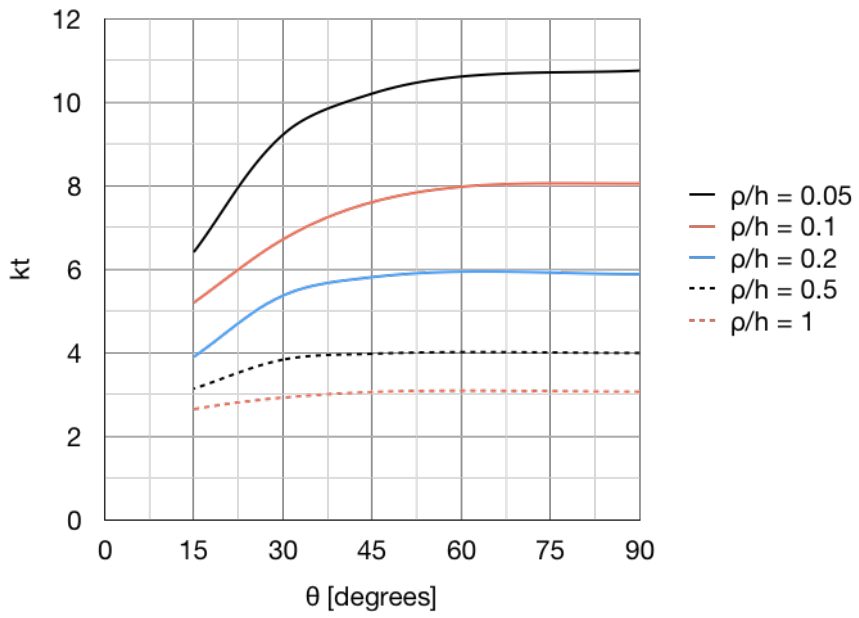

Figure 13: k_t of circular notches as a function of depth h, radius ρ, and notch angle θ [40].

2.5 Stress Concentration Factors

Before describing the simulations themselves, it is critical to note the difference between the various stress concentration factors and how this research uses them. k_t is a purely geometric, elastic stress concentration factor typically used for elastic loading. A notch or discontinuity with a stress concentration factor of 3 will increase the stress response at that point by a factor of three. This relation is used to establish loading limits, so a component does not surpass the material's ultimate strength, yield strength, safety factor, or other engineering limit.

While k_t is useful for elastic loadings, it does not apply when a cyclic load is applied. Under such conditions, localized plasticity or crack growth often occurs, reducing the intensity of the stress concentrator. In such cases, notch sensitivity q, a material and geometry dependent property, is used to modify k_t into k_f, or the fatigue stress concentration factor using equation (13). In general, $k_f < k_t$. One model to determine q is Peterson's equation, which uses the root radius ρ (used to calculate k_t) and a material property α, which can be a

function of the material's ultimate strength or its microstructure. In section 1.6, the α used was the width of the average acicular grain in the microstructure, measured to be 1.5 μm.

$$q = \frac{k_f - 1}{k_t - 1} \tag{13}$$

$$q = \frac{1}{1 + \frac{\alpha}{\rho}} \tag{14}$$

k_f is only constant at very high cycles. At lower cycles, it will vary depending on the load intensity. At or below low cycle failure ($N_f \approx 10^3$) k_f will approach 1, i.e., no stress concentration effects are present. At or above high cycle failure ($N_f \approx 10^7$), the stress concentration factor approaches the nominal k_f response. In order to account for all cycles, a simple logarithmic interpolation function approximates the response at medium cycles to failure into another term: $k_{f,real}$. Figure 14 and equation (16) summarizes these behaviors [41].

$$k_{f,real} = 1 + \frac{k_f - 1}{4} \log \frac{N_f}{10^3} \tag{15}$$

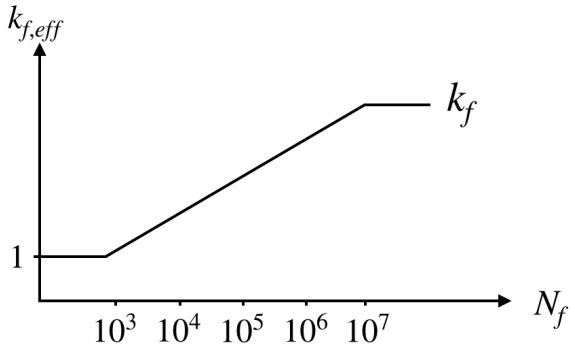

Figure 14: Variation of k_f in fatigue loading as the number of cycles to failure varies. (Graphic representation of equation (15)).

$$\text{Fatigue notch factor} = \begin{cases} 1 & N_f < 10^3 \\ k_{f,real} & 10^3 < N_f < 10^7 \\ k_f \text{ or } \bar{k}_t & N_f > 10^7 \end{cases} \tag{16}$$

Matching the data from Figure 8 using this method proves its effectiveness. Figure 8 used a different model of empirical relations based on the ultimate strength of the material at $N_f = 10^3$ and drawing a straight line to the run out stress. However, by varying the value of actual k_f using equation (15) and scaling the smooth loading curve by that factor, the accuracy of the model is improved, as shown in Figure 15.

In the Ansys simulations to follow, notches are defined geometrically using Figure 13 to produces a constant stress concentration factor. However, as described in Figure 14, fatigue notch factor effects will vary as the cycles to failure changes due to yielding, plasticity, crack growth, or other localized effects. None of these effects are present in an elastic finite element model, however. The fatigue notch factor effects of the notch will remain constant. As a result, data from notch simulations in this study should be considered lines of constant stress concentration, not realistic fatigue response. In Section 4.2, a data set from finite element analysis has equation (16) applied to it, producing a realistic response.

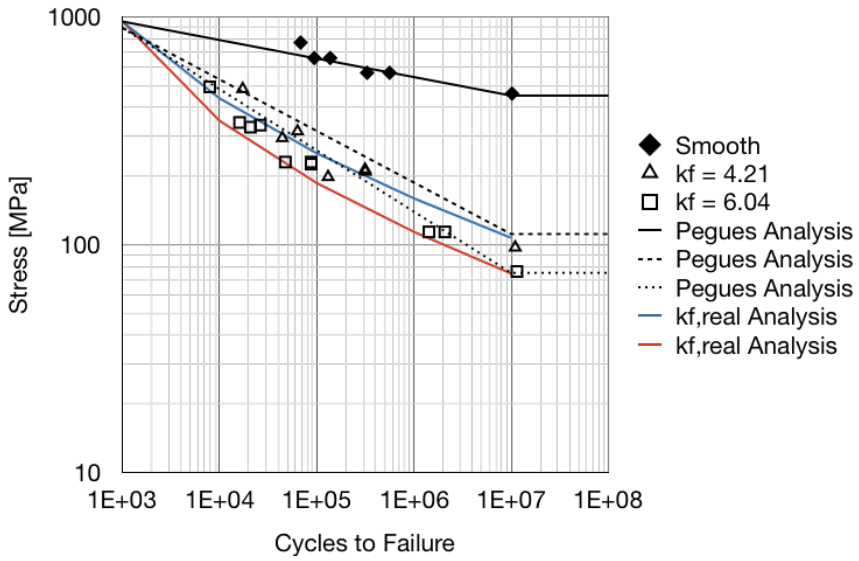

Figure 15: Matching fatigue life literature data of as-built Ti6Al4V using realistic $k_{f,real}$ analysis. (Data by Pegues [11]).

3 Simulation

The goal of this research is matching the S–N curve of a rough surface by modifying the strain life parameters. Simulations using Ansys Workbench are done to study representations of as-built, rough surface 3D printed Ti6Al4V, 7075-T6, and 4340 fatigue specimens, using material properties from Table 2. The geometry used is the axisymmetric model from ASTM E466–15. A 2D model saves significant computational time. Making the model symmetric about the center axis further reduces the node count. (For a representation of the meshing of a smooth specimen, see Figure 16.) Notches, when applied, are placed at the axis of symmetry at the center of the model. The Proximity and Curvature sizing model used for the simulation produces the best representation of the surface profiles compared to the other models, with and without notches. An all quad mesh is specified. A refinement factor of three, which splits one node into sixteen, is applied to the region expected to receive 50% of peak stress, which occurs within a depth approximately half the length of the applied notch feature into the part. In other words, if a notch extends 20 μm into the surface, a refinement is applied to a region extending 30 μm into the part. Lower refinement levels of two or one, producing a coarser mesh around the notch, varied the stress response of the model by less than 1%. Furthermore, a higher refinement level did not result in meaningfully longer solving times, so the higher refinement level of three was used. Mesh Defeaturing is disabled to retain fine roughness details on the surface. Fully reversed uniaxial loading is applied to produce S–N curves for each model. Material models use properties from Dowling [37].

Table 2: Material reference properties for FEA [37].

	Ti6Al4V	7075–T6	4340
σ'_f [MPa]	2030	1466	1758
b	-0.104	-0.143	-0.0977
ε'_f	0.841	0.262	2.12
c	-0.688	-0.619	-0.744
K' [MPa]	1772	977	1655
n'	0.106	0.106	0.131
E [GPa]	117	71	207
ρ [kg/m^3]	4620	2700	7870
ν	0.33	0.345	0.3

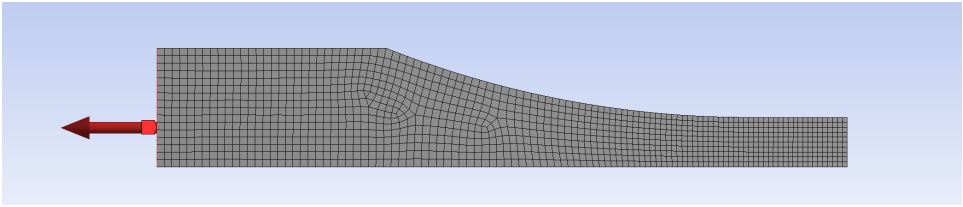

Figure 16: Axisymmetric/symmetric Ansys model with a smooth specimen, showing loading axis and mesh.

3.1 Initial Experiments

Initial simulations attempted to modify the surface of an axisymmetric specimen with a profile function resulting in a desired theoretical roughness. Models with a mathematically correct R_a and R_z/R_t were attempted using sine wave and with "stacked circle" constant radius surface discontinuity profiles, with the latter more closely matching the shape of flaws on the surface of a 3D printed part (Figure 4). However these tests were not successful. The sine wave profile, shown in Figures 17 and 18, had an infinite number of configurations which mathematically matched the roughness profile. The amplitude of the sine wave alone determined the R_a value and R_z/R_t value, with the wavelength of the sine wave having no effect on roughness calculation (see section 1.4). However, as the wavelength were varied,

different S–N results were produced. This behavior is shown in Figure 19, where a constant amplitude of 42 μm produced a roughness of $R_a = 26.7$ μm and $R_z = 21$ μm, but as the period length varied from 150 – 1000 μm, the S–N curve changed significantly.

The stacked circle profile is shown in Figure 20, and is defined by a male radius r_1 and a female radius r_2, as illustrated in the figure. Both radii could be independently varied. However, regardless of configuration of the radii, the S–N curves converged on an identical profile and did not match experimental data from literature, as shown in Figure 21. All configurations in the figure met the mathematical definition of $R_a = 26.7$ μm and $R_z = 21$ μm. This rapid convergence is explained by section 2.4. The stacked circle profile are effectively a series of circular notches with $\theta = 0$, as in Figure 12, being 0. At this θ level, stress concentrations converge at approximately 3 (as shown in Figure 13), meaning any circular notch with the same root depth will produce the same degree of amplified stress. The convergeant results in Figure 21 are therefore expected.

It was clear that although these regular geometric profiles matched the mathematical definition of roughness, they could not functionally or practically duplicate the random surface of as-built 3D printed metals. Matching R_a and R_z/R_t alone are not sufficient to describe the effects of roughness on fatigue life. Notches, applied to the model and calculated using effective stress concentration factor $\bar{k}_t$ (section 1.6) are a better way to represent roughness. Furthermore, as shown in Figure 22, a single sine wave produces an identical fatigue life result as several sine waves. Because of this, a single notch is deemed sufficient to produce a stress concentration effect for the following simulations to represent roughness.

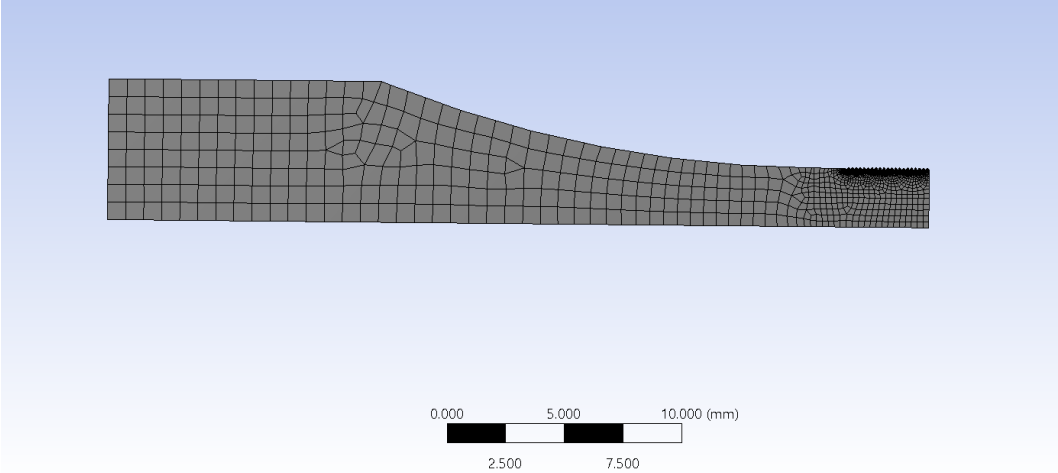

Figure 17: Axisymmetric fatigue testing model in Ansys, with mesh, showing sine wave roughness along the entire length of the testing region.

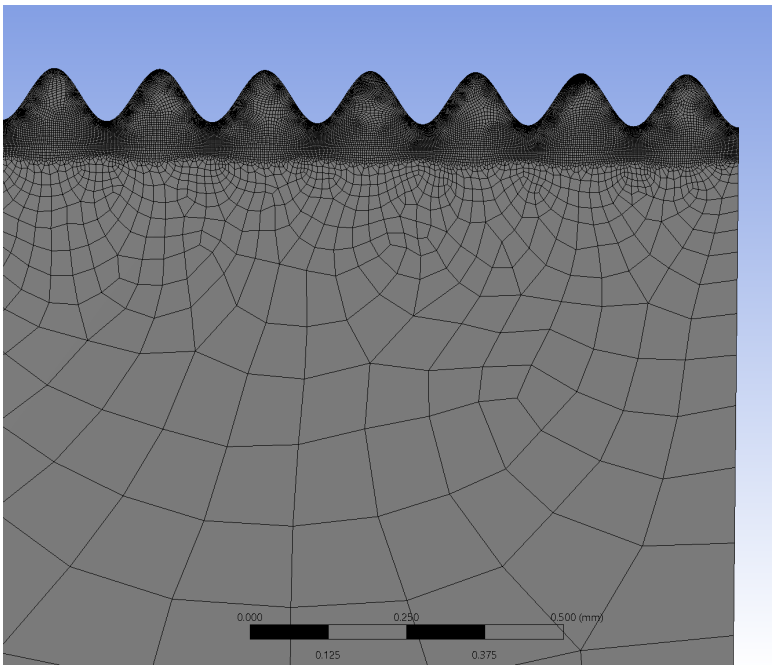

Figure 18: Meshing detail on a sine wave surface profile in Ansys (see Figure 17).

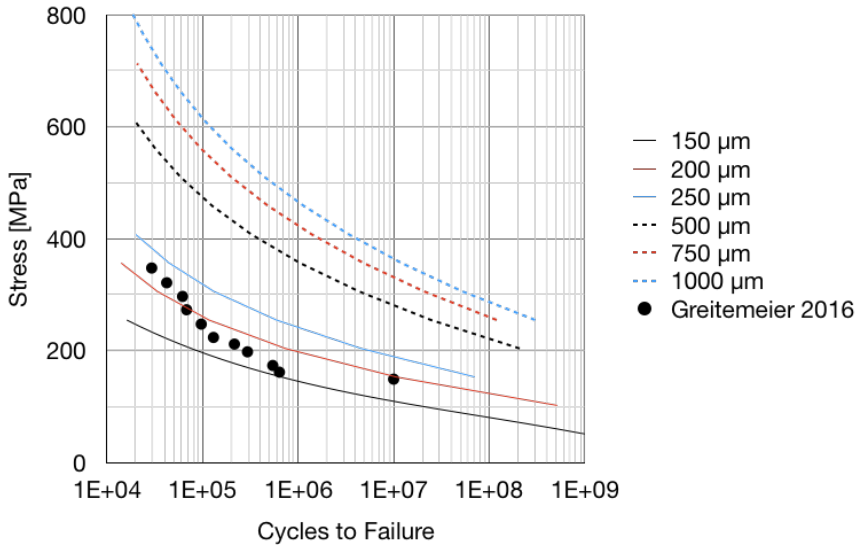

Figure 19: Comparing FEA results of a rough surface represented by a sine wave (amplitude 42 µm, period length 150–1000 µm) with roughness $R_a = 26.7$ µm and $R_z = 21$ µm, to experimental fatigue data of as-built 3D printed fatigue specimens from literature [26].

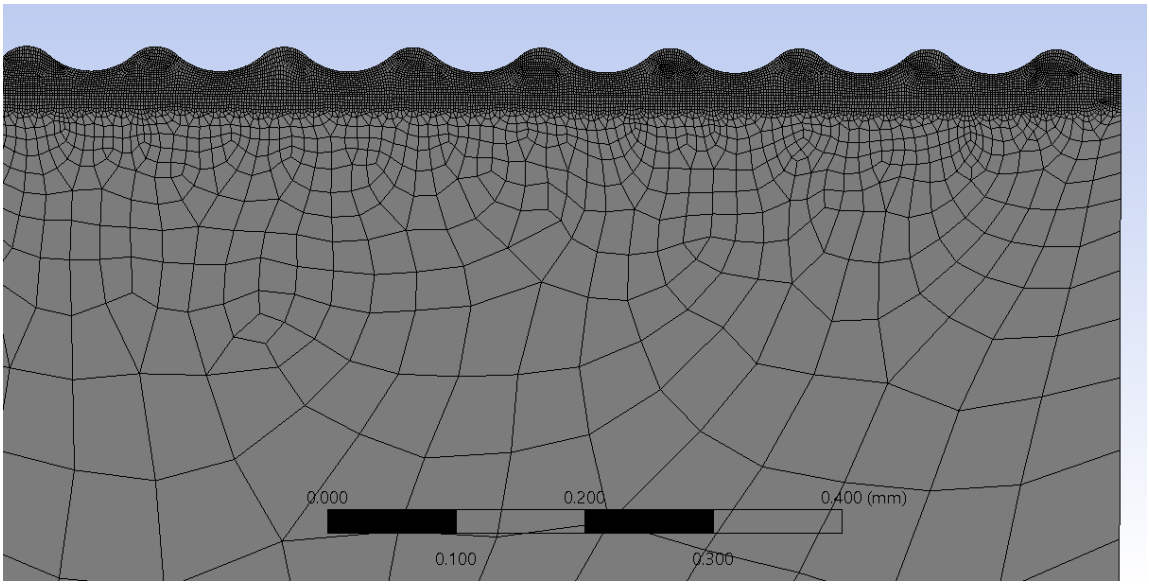

Figure 20: Meshing detail on a stacked circle surface profile. The male radius is r_1, the female radius is r_2.

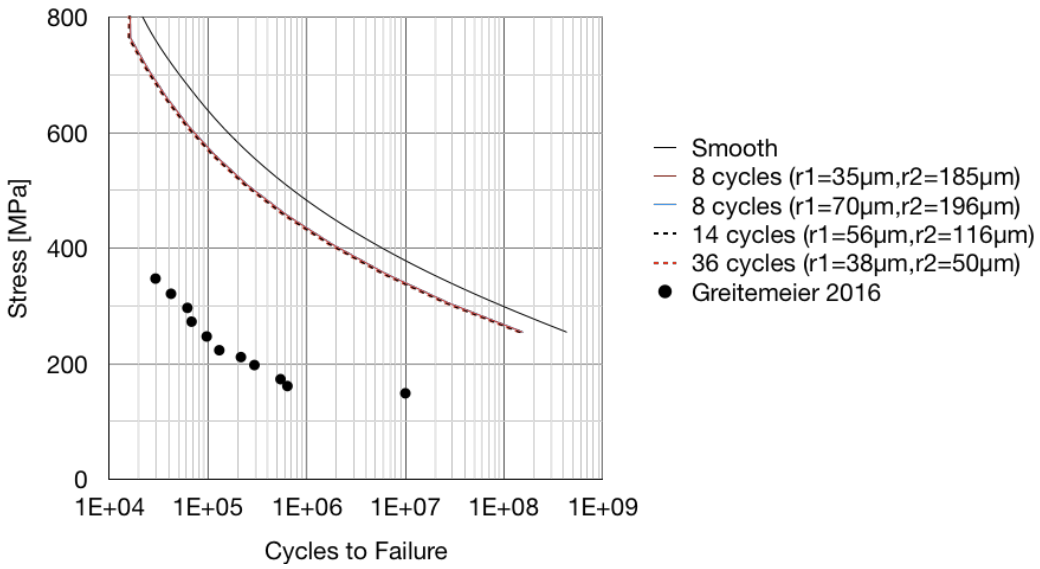

Figure 21: Comparing FEA results of a rough surface represented by stacked circles (varying r_1 and r_2 values) with roughness $R_a = 26.7$ µm and $R_z = 21$ µm, to experimental fatigue data of as-built 3D printed fatigue specimens from literature [26].

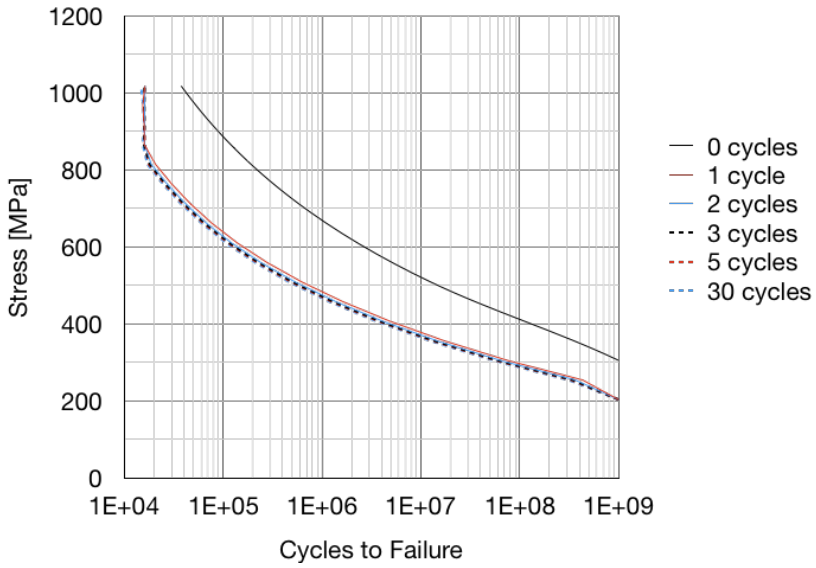

Figure 22: Convergence of the fatigue life curves for rough FEA models with a sine wave profile, as the number of sine wave cycles increases from 0 (smooth surface) to 30 cycles (total roughness along the shank).

3.2 Parametric Study

The first part of this study examines the effects of strain life parameters σ'_f, b, ε'_f, and c on a smooth FEA model to illustrate the transformative effects they have on an S–N curve. Although the trends may be guessed based on Figure 9, it is still necessary to determine accurate data for a stress-controlled experiment rather than for strain, as shown in the figure. A smooth axisymmetric model is used with the omission of any refinements, as there are no notches or areas of increased stress in the smooth model. A baseline S–N curve for the three materials is established using properties from Table 2. From there, the four strain life parameters are varied and plotted to determine their transformative effects on the S–N curve. The parametric variation of Ti6Al4V strain life parameters is shown in Figures 23 through 26.

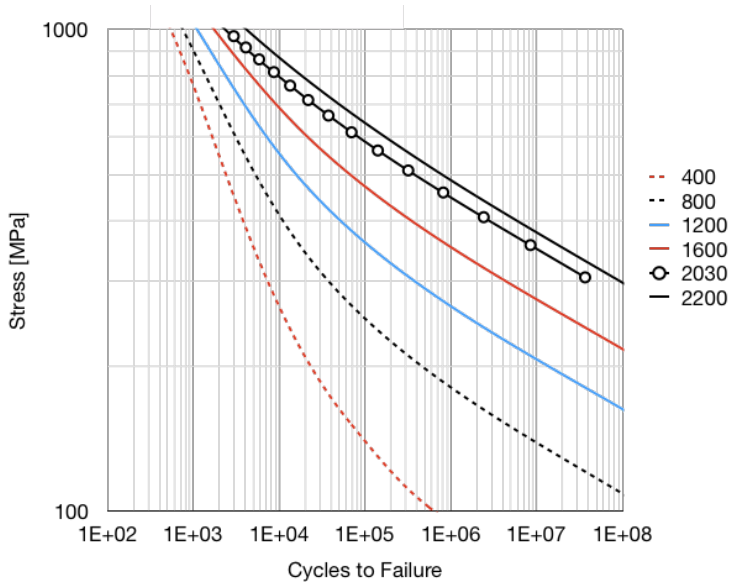

Figure 23: Effects of σ'_f on S–N curve of Ti6Al4V.

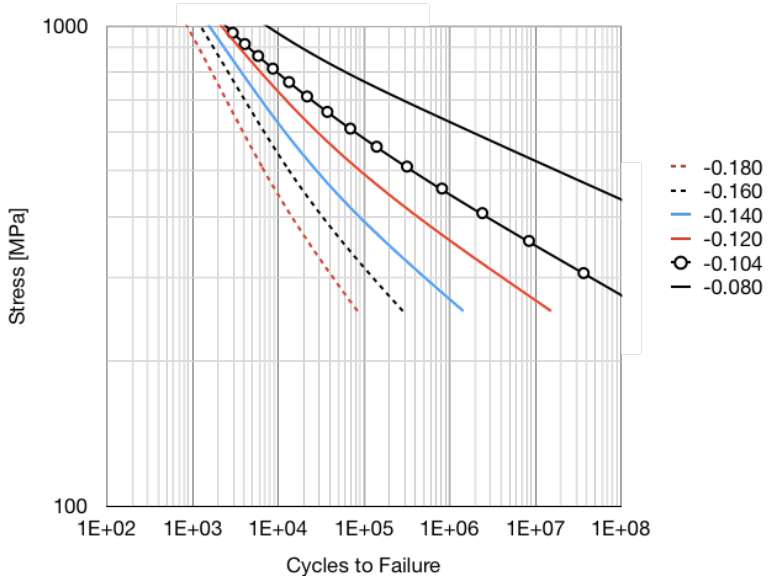

Figure 24: Effects of b on S–N curve of Ti6Al4V.

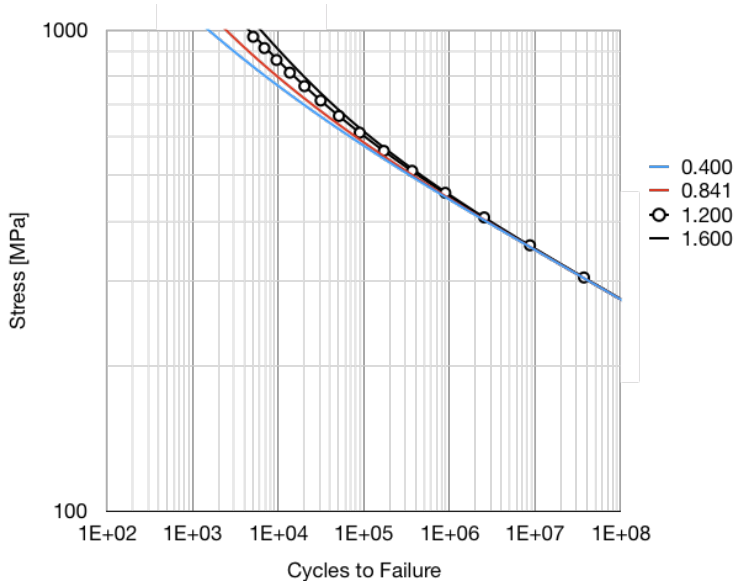

Figure 25: Effects of ε_f' on S–N curve of Ti6Al4V.

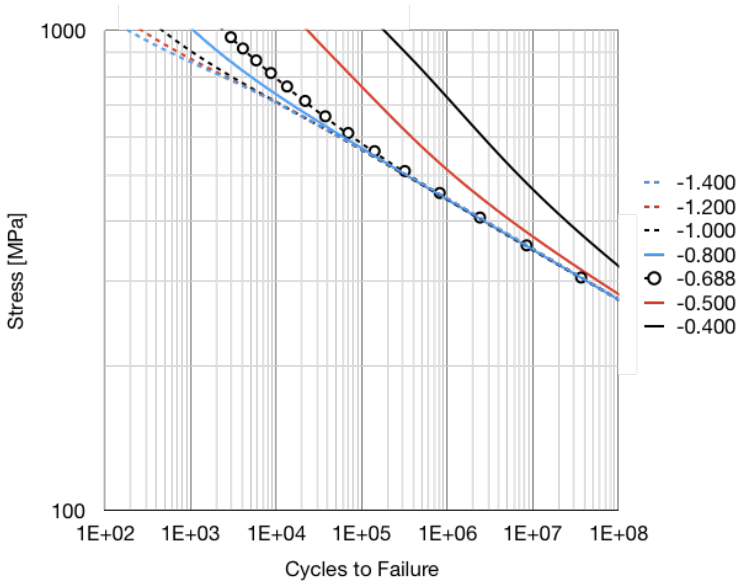

Figure 26: Effects of c on S–N curve of Ti6Al4V.

Analysis of Figures 23 through 26 reveals overall trends. σ'_f generally affects the intercept at lower stresses to failure, ε'_f generally affects the intercept at higher stresses to failure, and b and c deal primarily with the slope of the curve in those respective regions. Initial experiments in notch S–N response (section 3.3 reveal that stress concentration factors do not substantially change the S-N slope, but the graph does translate up and down significantly. Further strain life modifications omit b and c from consideration because they primarily concern slope. They are held constant at their reference values for all further simulations.

3.3 Notched Models

Simulations into the effects of notches on the S–N curve establishes a baseline of constant stress concentration effects. Equation (4) shows that $\bar{k}_t$ can sufficiently represent roughness effects on fatigue life. Notched models are created in Ansys using the procedure above with geometry, as described in section 2.4. Circular, $\theta = 90°$ notches with k_t values of 3.058, 3.988, 5.878, 8.044, and 10.750 are applied to the center of the models at the point of peak expected stress. The simulation of notched models with standard material properties

produces S–N curves of constant stress concentration for the three materials described above, shown in Figures 27 through 29.

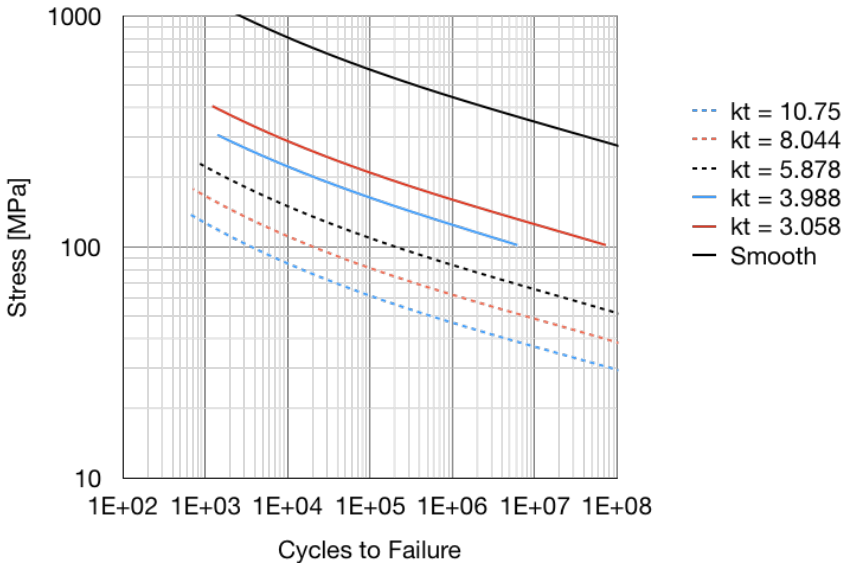

Figure 27: Effects of notches on S–N curve for Ti6Al4V.

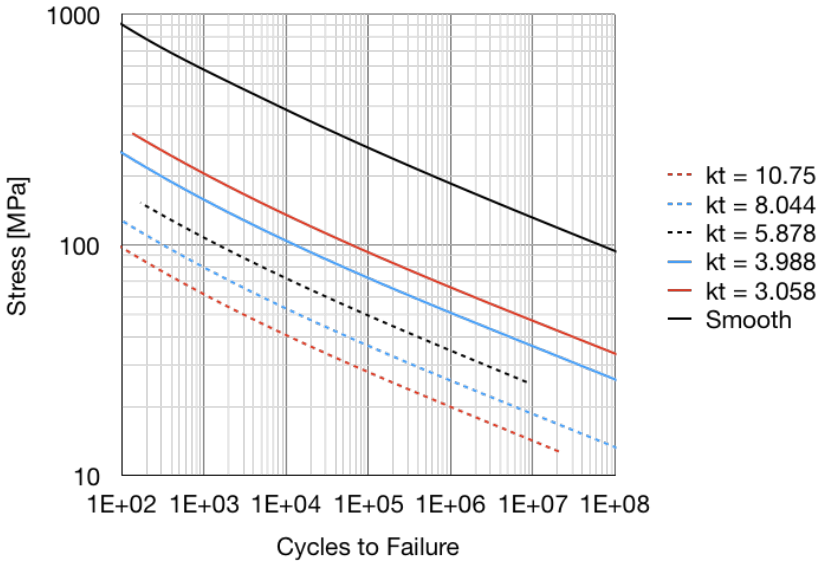

Figure 28: Effects of notches on S–N curve for 7075–T6.

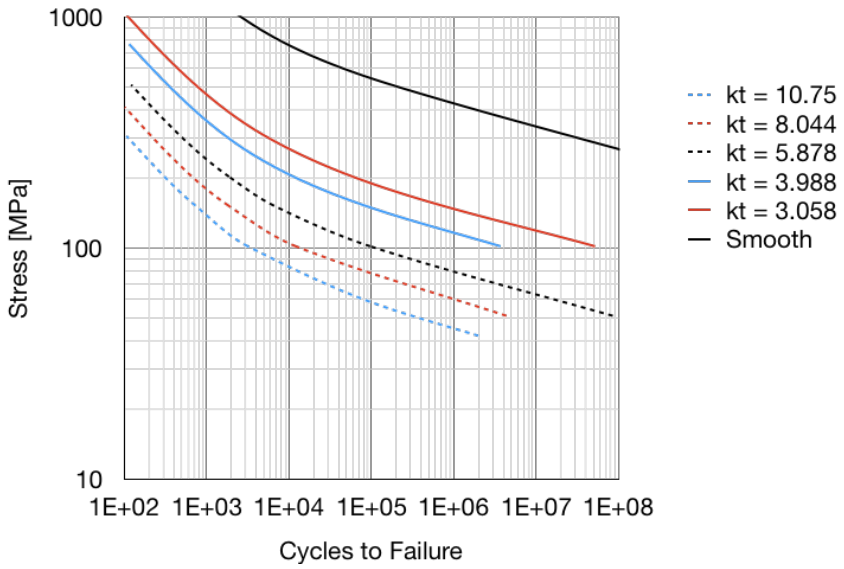

Figure 29: Effects of notches on S–N curve for 4340.

3.4 Matching Notches With Modified Strain Life

Reproducing the S–N curves shown in Figures 27 through 29 is possible with a using a smooth specimen and by by modifying strain life parameters σ_f' and ε_f' as in section 3.2. Accuracy of the modified S–N curves defined as the minimum magnitude of variance from the notched S–N curves, with precision of the modified strain life properties carried out to a maximum of three significant figures of precision. Through significant simulation, Figure 30 is obtained using this procedure (see Appendix D for aluminum and steel). Table 3 summarizes the modified strain life parameters, $\sigma_f'^*$ and $\varepsilon_f'^*$, used to obtain the S–N curves for all stress concentration factors.

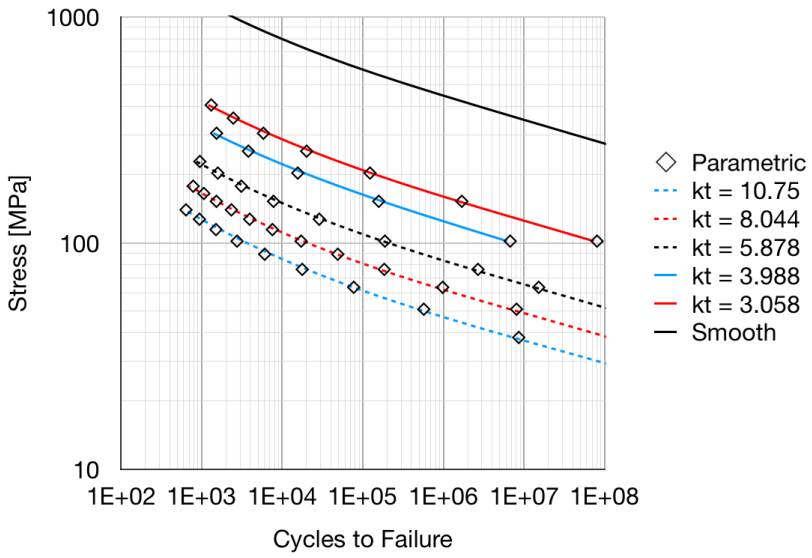

Figure 30: Matching S–N curve of notched Ti6Al4V using $\sigma_f'^*$ and $\varepsilon_f'^*$.

Table 3: Parametrically determined strain life terms, $\sigma_f'^*$ and $\varepsilon_f'^*$, to match notches in S–N curve.

	Ti6Al4V		7075–T6		4340	
k_t	$\sigma_f'^*$	$\varepsilon_f'^*$	$\sigma_f'^*$	$\varepsilon_f'^*$	$\sigma_f'^*$	$\varepsilon_f'^*$
1.000	2030	0.841	1466	0.262	1758	2.12
3.058	735	0.180	540	0.028	627	0.275
3.988	567	0.135	417	0.0262	487	0.210
5.878	386	0.0860	285	0.0172	334	0.129
8.044	289	0.0620	212	0.0130	250	0.0920
10.75	218	0.0450	159	0.00870	189	0.0600

4 Analysis

4.1 Matching S–N Curve

Data from Table 3 accurately matches the S–N curve of notched fatigue samples in FEA simulation for only the stress concentration factors tested. In order to determine an S–N curve for any constant stress concentration, regression analysis is done to identify trends in this table.

Figures 31 and 32 show a plot of $\sigma_f'^*$ and $\varepsilon_f'^*$ with respect to $\bar{k}_t$. The curves produced with this data strongly correlates with power law regression (see Appendix B for all). However, there is some divergence, particularly as $\bar{k}_t$ approaches one, where the modified strain life parameters should approach the reference σ_f' and ε_f'. A correction factor is introduced to account for this, shown as the second term in equations (17) and (18), which reduces the variable count and increases accuracy as ($\bar{k}_t \to 1$).

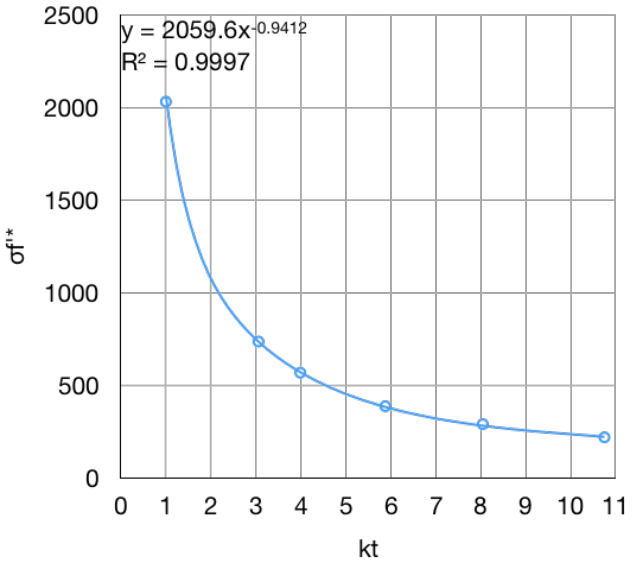

Figure 31: Trends of $\sigma_f'^*$ for Ti6Al4V (Power Law Regression).

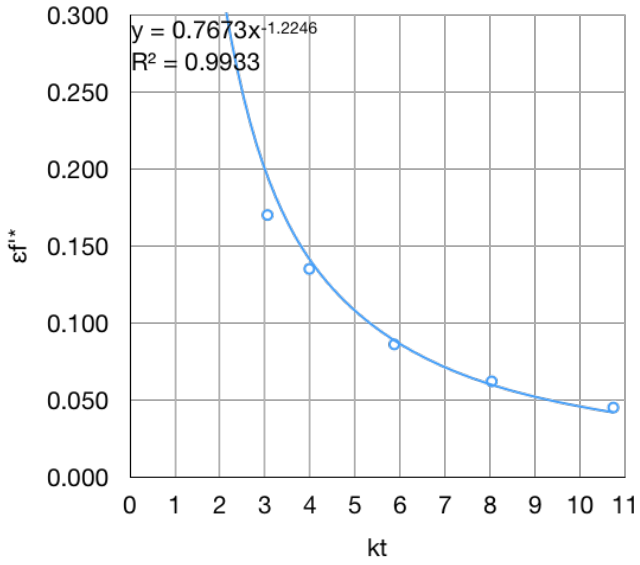

Figure 32: Trends of $\varepsilon_f'^*$ for Ti6Al4V (Power Law Regression).

$$\bar{\sigma}_f' = \sigma_f' \left(\bar{k}_t\right)^d + \frac{1}{f\left(\bar{k}_t - 1\right)^g} \quad \left(\bar{k}_t \neq 1\right) \tag{17}$$

$$\bar{\varepsilon}_f' = \varepsilon_f' \left(\bar{k}_t\right)^j + \frac{1}{m\left(\bar{k}_t - 1\right)^p} \quad \left(\bar{k}_t \neq 1\right) \tag{18}$$

Steps 1 through 10 describe the procedure for determining parameters for equations (17) and (18). For tabulated steps for all materials, see Appendices A through C.

1. Plot $\sigma_f'^*$ and $\varepsilon_f'^*$ against $\bar{k}_t$; perform power law regression.
2. Take the exponent of this regression to be d and j for σ and ε, respectively.
3. Replace the coefficient of this regression with the original σ_f' and ε_f' from Table 2.
4. Using the coefficient and exponent from steps 2–3, produce a list of predicted initial terms: $\sigma_f'^i$ and $\varepsilon_f'^i$, as in equation (19).
5. The differences between $\sigma_f'^i$ and $\varepsilon_f'^i$ and $\sigma_f'^*$ and $\varepsilon_f'^*$ terms are called the correction factors, δ, as in equation (20).
6. Take the inverse of delta and graph against $(\bar{k}_t - 1)$. Perform power law regression as in Figures 33 and 34.

7. Take the coefficient of the step 6 regression to be f and k for σ and ε, respectively.
8. Take the exponent of the step 6 regression to be g and m for σ and ε, respectively.
9. A list of predicted correction terms, $\sigma_f'^{\delta}$ and $\varepsilon_f'^{\delta}$, is produced from the inverse of this regression, shown in equation (21).
10. The difference between the initial terms and correction terms is the final result: $\bar{\sigma}_f'$ and $\bar{\varepsilon}_f'$, as in equation (22).

$$\sigma_f'^{i} = \sigma_f' \left(\bar{k}_t\right)^d \quad , \quad \varepsilon_f'^{i} = \varepsilon_f' \left(\bar{k}_t\right)^j \tag{19}$$

$$\delta = \sigma_f'^{i} - \sigma_f'^{*} \quad , \quad \delta = \varepsilon_f'^{i} - \varepsilon_f'^{*} \tag{20}$$

$$\sigma_f'^{\delta} = \frac{1}{f\left(\bar{k}_t - 1\right)^g} \quad , \quad \varepsilon_f'^{\delta} = \frac{1}{m\left(\bar{k}_t - 1\right)^p} \tag{21}$$

$$\bar{\sigma}_f' = \bar{\sigma}_f'^{i} - \bar{\sigma}_f'^{\delta} \quad , \quad \bar{\varepsilon}_f' = \bar{\varepsilon}_f'^{i} - \bar{\varepsilon}_f'^{\delta} \tag{22}$$

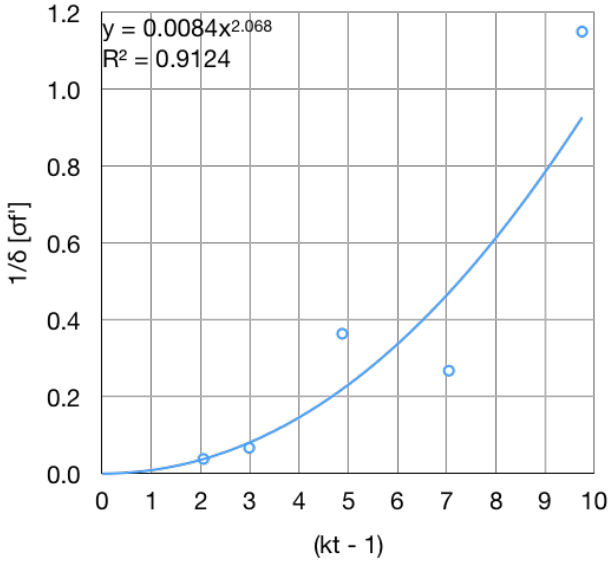

Figure 33: Inverse of correction factor of $\sigma_f'^{*}$ for Ti6Al4V (power law regression), computing parameters f and g.

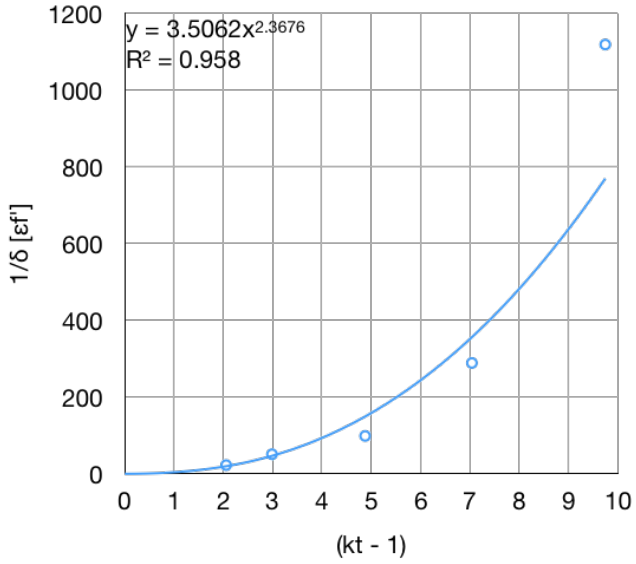

Figure 34: Inverse of correction factor of $\varepsilon_f'^*$ for Ti6Al4V (power law regression), computing parameters m and p.

Table 4 demonstrates the effectiveness of this method in FEA for titanium ε_f' analysis. Where the initial $\varepsilon_f'^i$ term varied from the known $\varepsilon_f'^*$ by up to 48%, the addition of $\varepsilon_f'^\delta$ reduced the error to 4.5%. Table 5 shows all variables required for equations (17) and (18). Figure 35 compares the notched FEA models to smooth models using the calculated $\bar{\sigma}_f'$ and $\bar{\varepsilon}_f'$ and parameters from equations (17) and (18). (For $\bar{\sigma}_f'$, and other materials, see Appendix D). With this correction factor, the list of parametrically determined strain life terms are able to be reproduced accurately for any stress concentration factor in the ranges tested.

Table 4: Process for determining $\bar{\varepsilon}_f'$ for Ti6Al4V, illustrating error correction effectiveness.

k_t	$\varepsilon_f'^*$	$\varepsilon_f'^i$	δ	$1/\delta$	(k_t - 1)	$\varepsilon_f'^\delta$	$\bar{\varepsilon}_f'$	% error
1.000	0.841	0.841	0		0.000		0.841	0.00%
3.058	0.170	0.2140	0.04396	22.74	2.058	0.05165	0.162	4.52%
3.988	0.135	0.1546	0.01957	51.10	2.988	0.02136	0.133	1.33%
5.878	0.0860	0.09612	0.01012	98.82	4.878	0.006694	0.0894	3.98%
8.044	0.0620	0.06546	0.003459	289.1	7.044	0.002805	0.0627	1.06%
10.75	0.0450	0.04589	0.0008936	1119	9.75	0.001299	0.0446	0.90%

Table 5: Modified strain life parameters for use with equations (17) and (18).

	Ti6Al4V	7075–T6	4340
d	-0.941	-0.936	-0.940
j	-1.22	-1.39	-1.48
f	0.00835	0.00376	0.155
m	-3.51	-7.37	-1.18
g	2.07	2.68	1.02
p	2.37	2.17	2.41

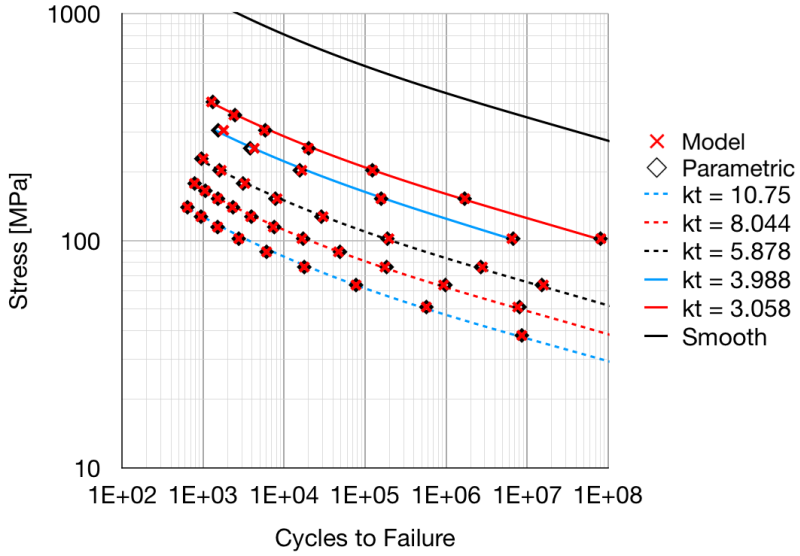

Figure 35: S–N comparison between smooth, notched, and smooth with computed $\bar{\sigma}'_f$ and $\bar{\varepsilon}'_f$ for Ti6Al4V.

4.2 Realistic S–N Modeling

Figure 35 illustrates the correlation between equations (17) and (18) and parametrically determined variables from FEA simulation. Though, as described in section 2.5, it only shows lines of constant stress concentration. Equation (16) must be applied to account for stress concentration variance. Assuming a nominal k_f of 10.75, a curve of realistic S–N response is drawn using equation (15), connecting between points of constant stress concentration. The curve illustrates a realistic response expected from physical

experimentation. Data from Figure 8 can also be added to compare experimental results. The nominal k_f is taken to be 4.21 and 6.04, as from the experiment. (See Appendix D for other materials without literature comparison).

Figure 36 provides a summary of this for Ti6Al4V. Lines of constant stress concentration 10.75, 8.044, 5.878, 3.988, and 3.058 from notched FEA models is shown, as well as a smooth FEA model (section 3.3). Parametric data points from section 3.4 are graphed as diamonds. Data points using equations (17) and (18) (section 4.1) are shown as x's. Experimental data from Pegues, Roach, and Williamson [11] (section 1.6) is plotted as circles, filled circles, and filled squares. Finally, the experimental data is matched by connecting the lines of constant stress concentration as described by the realistic fatigue stress concentration effect in equation (16) (section 2.5) using thick black and blue lines. A predicted response for $k_t = 10.75$ is also shown. The realistic response correlates graphically with the experimental data, illustrating the viability of this procedure.

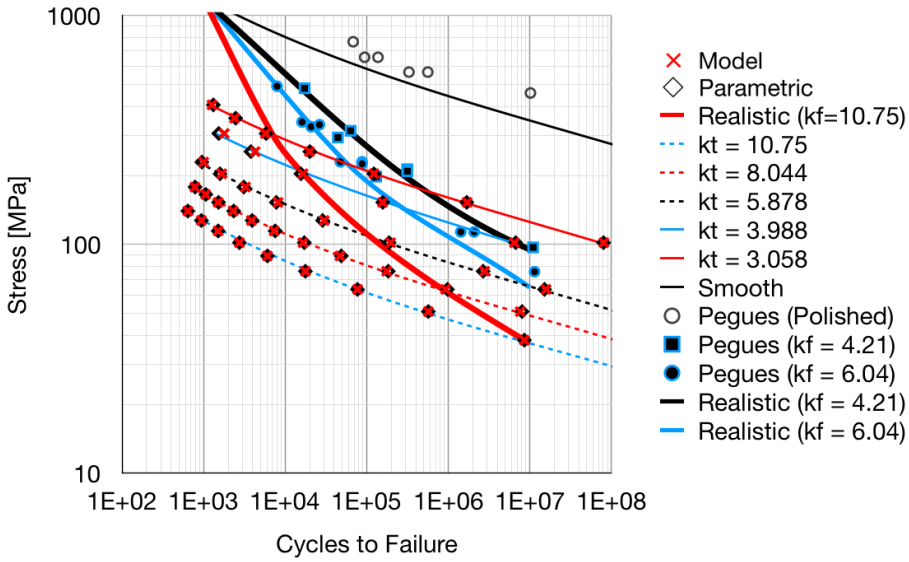

Figure 36: S–N comparison between smooth, notched, and smooth with computed $\bar{\sigma}'_f$ and $\bar{\varepsilon}'_f$ for Ti6Al4V, with realistic S–N response for a varying k_f, compared to literature [11].

5 Conclusions

This research proposes a model for representing the effects of stress concentration factors on fatigue life through modified strain life parameters. 3D printed components, in their as-built state, have extremely rough surfaces, which contribute significantly to the up to 50% lower fatigue life compared to standard materials. Literature has shown that these materials can have their roughnesses expressed as an effective stress concentration factor with reasonably good accuracy in predicting fatigue life.

When a finite element model expresses an effective stress concentration factor as a physical notch, the S–N curve shifts downward. Modifying σ'_f and ε'_f in a strain life analysis replicates this curve shift, and equations are derived to reproduce those results for constant stress concentration factors of any range. A model that replicates realistic variation in stress concentration is applied to connect the lines of constant stress concentration. The curves of experimental data from literature and realistic FEA results align and perform as expected when plotted together, demonstrating their effectiveness.

With this method, the fatigue life of as-built 3D printed metals can be easily predicted using FEA or any other analysis. The model is effective for titanium, aluminum, and steel. The six parameters used in the model are material dependent and can be determined using simulation. Additional physical experimentation using as-built 3D printed specimens and known material properties may increase the accuracy of the model and verify its integrity.

The fatigue life of components with significant surface roughness can be predicted by measuring the roughness data and applying the equations above. Components with complex geometries can be analyzed using FEA as quickly as simple ones and without applying notches or any modifications to the geometry or mesh. All that is required is to measure the surface roughness and change the strain life parameters. This research can accelerate fatigue analysis of as-built 3D printed parts, adding another tool to fatigue life prediction of complex parts other than physical testing.

REFERENCES

Frazier, W. E. (2014). Metal additive manufacturing: A review.
Journal of Materials Engineering and Performance, *23*(6), 1917–1928.
doi:10.1007/s11665-014-0958-z

Seifi, M., Gorelik, M., Waller, J., Hrabe, N., Shamsaei, N., Daniewicz, S., and Lewandowski, J. J. (2017). Progress towards metal additive manufacturing standardization to support qualification and certification.
Journal of The Minerals, *69*(3), 439–455. doi:10.1007/s11837-017-2265-2

Bikas, H., Stavropoulos, P., and Chryssolouris, G. (2016).
Additive manufacturing methods and modelling approaches: A critical review.
The International Journal of Advanced Manufacturing Technology, *83*(1-4), 389–405.
doi:10.1007/s00170-015-7576-2

Cao, F., Zhang, T., Ryder, M. A., and Lados, D. A. (2018).
A review of the fatigue properties of additively manufactured ti-6al-4v.
Journal of The Minerals, *70*(3), 349–357. doi:10.1007/s11837-017-2728-5

Yadollahi, A., and Shamsaei, N. (2017).
Additive manufacturing of fatigue resistant materials: Challenges and opportunities.
International Journal of Fatigue, *98*, 14–31.
doi:https://doi.org/10.1016/j.ijfatigue.2017.01.001

Yadolla, A., Mahtabi, M., Khalili, A., Doude, H., and Newman Jr, J. (2018).
Fatigue life prediction of additively manufactured material: Effects of surface roughness, defect size, and shape.
Fatigue & Fracture of Engineering Materials & Structures, *41*(7), 1602–1614.
doi:10.1111/ffe.12799

Nicoletto, G., Konečná, R., Frkáň, M., and Riva, E. (2018).
Surface roughness and directional fatigue behavior of as-built ebm and dmls ti6al4v.

International Journal of Fatigue, *116*, 140–148.
doi:https://doi.org/10.1016/j.ijfatigue.2018.06.011

Thompson, M. (2006). Methods for generating rough surfaces in ansys. In *Proceedings of the 2006 international ansys users conference & exhibition, pittsburgh, pa*.

Thompson, M., Thompson, J., and Slocum, A. (2007).
Surface topography importation in finite element models.
In *Proceedings of the 7th international conference for the european society for precision engineering and nanotechnology* (Vol. 1, pp. 373–376).

Thompson, M., and Thompson, J. (2010).
Methods for generating probabilistic rough surfaces in ansys.
In *Proc. 20th korea ansys user's conf* (pp. 9–10).

Pegues, J. W., Shamsaei, N., Roach, M. D., and Williamson, R. S. (2019).
Fatigue life estimation of additive manufactured parts in the as-built surface condition.
Material Design & Processing Communications, *1*(3), e36. e36 MDPC-2018-025.R1.
doi:10.1002/mdp2.36

Kruth, J.-P. (1991). Material incress manufacturing by rapid prototyping techniques.
International Academy for Production Engineering Annals-Manufacturing Technology, *40*(2), 603–614.

Sterling, A., Shamsaei, N., Torries, B., and Thompson, S. M. (2015).
Fatigue behaviour of additively manufactured ti-6al-4 v. *Procedia Engineering*, *133*, 576–589.

Sterling, A. J., Torries, B., Shamsaei, N., Thompson, S. M., and Seely, D. W. (2016).
Fatigue behavior and failure mechanisms of direct laser deposited ti–6al–4v.
Materials Science and Engineering: A, *655*, 100–112.

Zhai, Y., Lados, D. A., Brown, E. J., and Vigilante, G. N. (2016).
Fatigue crack growth behavior and microstructural mechanisms in ti-6al-4v

manufactured by laser engineered net shaping. *International Journal of Fatigue*, *93*, 51–63. doi:https://doi.org/10.1016/j.ijfatigue.2016.08.009

Zhai, Y., Galarraga, H., and Lados, D. A. (2015). Microstructure evolution, tensile properties, and fatigue damage mechanisms in ti-6al-4v alloys fabricated by two additive manufacturing techniques. *Procedia Engineering*, *114*, 658–666. ICSI 2015 The 1st International Conference on Structural Integrity Funchal, Madeira, Portugal 1st to 4th September, 2015. doi:https://doi.org/10.1016/j.proeng.2015.08.007

Leuders, S., Thöne, M., Riemer, A., Niendorf, T., Tröster, T., Richard, H., and Maier, H. (2013). On the mechanical behaviour of titanium alloy tial6v4 manufactured by selective laser melting: Fatigue resistance and crack growth performance. *International Journal of Fatigue*, *48*, 300–307. doi:https://doi.org/10.1016/j.ijfatigue.2012.11.011

Günther, J., Krewerth, D., Lippmann, T., Leuders, S., Tröster, T., Weidner, A., ... Niendorf, T. (2017). Fatigue life of additively manufactured ti–6al–4v in the very high cycle fatigue regime. *International Journal of Fatigue*, *94*, 236–245. Fatigue and Fracture Behavior of Additive Manufactured Parts. doi:https://doi.org/10.1016/j.ijfatigue.2016.05.018

Greitemeier, D., Palm, F., Syassen, F., and Melz, T. (2017). Fatigue performance of additive manufactured tial6v4 using electron and laser beam melting. *International Journal of Fatigue*, *94*, 211–217. Fatigue and Fracture Behavior of Additive Manufactured Parts. doi:https://doi.org/10.1016/j.ijfatigue.2016.05.001

Edwards, P., and Ramulu, M. (2014). Fatigue performance evaluation of selective laser melted ti–6al–4v.

Materials Science and Engineering: A, *598*, 327–337.
doi:https://doi.org/10.1016/j.msea.2014.01.041

Wycisk, E., Emmelmann, C., Siddique, S., and Walther, F. (2013). High cycle fatigue (hcf) performance of ti-6al-4v alloy processed by selective laser melting.
In *Manufacturing science and technology (icmst2013)* (Vol. 816, pp. 134–139). Advanced Materials Research. doi:10.4028/www.scientific.net/AMR.816-817.134

Zhao, S., Li, S., Hou, W., Hao, Y., Yang, R., and Misra, R. (2016).
The influence of cell morphology on the compressive fatigue behavior of ti-6al-4v meshes fabricated by electron beam melting.
Journal of the Mechanical Behavior of Biomedical Materials, *59*, 251–264.
doi:https://doi.org/10.1016/j.jmbbm.2016.01.034

Günther, J., Leuders, S., Koppa, P., Tröster, T., Henkel, S., Biermann, H., and Niendorf, T. (2018). On the effect of internal channels and surface roughness on the high-cycle fatigue performance of ti-6al-4v processed by slm. *Materials& Design*, *143*, 1–11.
doi:https://doi.org/10.1016/j.matdes.2018.01.042

Gong, H., Rafi, K., Gu, H., Ram, G. J., Starr, T., and Stucker, B. (2015).
Influence of defects on mechanical properties of ti–6al–4v components produced by selective laser melting and electron beam melting. *Materials& Design*, *86*, 545–554.
doi:https://doi.org/10.1016/j.matdes.2015.07.147

Nicoletto, G. (2018).
Efficient determination of influence factors in fatigue of additive manufactured metals.
Procedia Structural Integrity, *8*, 184–191. AIAS2017 - 46th Conference on Stress Analysis and Mechanical Engineering Design, 6-9 September 2017, Pisa, Italy.
doi:https://doi.org/10.1016/j.prostr.2017.12.020

Greitemeier, D., Donne, C. D., Syassen, F., Eufinger, J., and Melz, T. (2016).
Effect of surface roughness on fatigue performance of additive manufactured ti–6al–4v.

Materials Science and Technology, *32*(7), 629–634.
doi:10.1179/1743284715Y.0000000053

Liu, J., Yue, Z., and Liu, Y. (2007). Surface finish of open holes on fatigue life.
Theoretical and Applied Fracture Mechanics, *47*(1), 35–45.
doi:https://doi.org/10.1016/j.tafmec.2006.10.008

Edwards, P., O'Conner, A., and Ramulu, M. (2013). Electron beam additive manufacturing of titanium components: Properties and performance.
Journal of Manufacturing Science and Engineering, *135*(6). 061016.
doi:10.1115/1.4025773

Kahlin, M., Ansell, H., and Moverare, J. (2017a).
Fatigue behaviour of notched additive manufactured ti6al4v with as-built surfaces.
International Journal of Fatigue, *101*, 51–60.
doi:https://doi.org/10.1016/j.ijfatigue.2017.04.009

Kahlin, M., Ansell, H., and Moverare, J. (2017b). Fatigue behaviour of additive manufactured ti6al4v, with as-built surfaces, exposed to variable amplitude loading.
International Journal of Fatigue, *103*, 353–362.
doi:https://doi.org/10.1016/j.ijfatigue.2017.06.023

Beretta, S., and Romano, S. (2017). A comparison of fatigue strength sensitivity to defects for materials manufactured by am or traditional processes.
International Journal of Fatigue, *94*, 178–191.
Fatigue and Fracture Behavior of Additive Manufactured Parts.
doi:https://doi.org/10.1016/j.ijfatigue.2016.06.020

Ahn, D., Kweon, J.-H., Kwon, S., Song, J., and Lee, S. (2009).
Representation of surface roughness in fused deposition modeling.
Journal of Materials Processing Technology, *209*(15), 5593–5600.
doi:https://doi.org/10.1016/j.jmatprotec.2009.05.016

Ahn, D., Kim, H., and Lee, S. (2009). Surface roughness prediction using measured data and interpolation in layered manufacturing.
Journal of Materials Processing Technology, *209*(2), 664–671.
doi:https://doi.org/10.1016/j.jmatprotec.2008.02.050

Kaji, F., and Barari, A. (2015). Evaluation of the surface roughness of additive manufacturing parts based on the modelling of cusp geometry.
International Federation of Automatic Control-PapersOnLine, *48*(3), 658–663.
15th International Federation of Automatic Control Symposium onInformation Control Problems inManufacturing. doi:https://doi.org/10.1016/j.ifacol.2015.06.157

Strano, G., Hao, L., Everson, R. M., and Evans, K. E. (2013).
Surface roughness analysis, modelling and prediction in selective laser melting.
Journal of Materials Processing Technology, *213*(4), 589–597.
doi:https://doi.org/10.1016/j.jmatprotec.2012.11.011

Browell, R., and Hancq, A. (2006). Calculating and displaying fatigue results. *Ansys Inc*, *2*.

Dowling, N. E. (2013). *Mechanical behavior of materials: Engineering methods for deformation, fracture, and fatigue* (4th). Pearson.

Lee, H.-H. (2018). *Finite element simulations with ansys workbench 18*. SDC publications.

Astm e466-15, standard practice for conducting force controlled constant amplitude axial fatigue tests of metallic materials. (2015). ASTM International. West Conshohocken, PA.
Retrieved from www.astm.org

Nowell, D., Dini, D., and Duó, P. (2003). Stress analysis of v-notches with and without cracks, with application to foreign object damage.
The Journal of Strain Analysis for Engineering Design, *38*(5), 429–441.
doi:10.1243/03093240360713487

Kujawski, D. (2019). *Personal communication*. Western Michigan University.

A Modified Strain Life Procedures

Table 6: Process for determining $\bar{\sigma}'_f$ for Ti6Al4V, illustrating error correction effectiveness.

k_t	σ'^{*}_f	σ'^{i}_f	δ	$1/\delta$	(k_t - 1)	σ'^{δ}_f	$\bar{\sigma}'^{i}_f$	% error
1.000	0.841	0.841	0		0.000		0.841	0.00%
3.058	0.170	0.2140	0.04396	22.74	2.058	0.05165	0.162	4.52%
3.988	0.135	0.1546	0.01957	51.10	2.988	0.02136	0.133	1.33%
5.878	0.0860	0.09612	0.01012	98.82	4.878	0.006694	0.0894	3.98%
8.044	0.0620	0.06546	0.003459	289.1	7.044	0.002805	0.0627	1.06%
10.75	0.0450	0.04589	0.0008936	1119	9.75	0.001299	0.0446	0.90%

Table 7: Process for determining $\bar{\varepsilon}'_f$ for Ti6Al4V, illustrating error correction effectiveness.

k_t	ε'^{*}_f	ε'^{i}_f	δ	$1/\delta$	(k_t - 1)	ε'^{δ}_f	$\bar{\varepsilon}'^{i}_f$	% error
1.000	0.841	0.841	0		0.000		0.841	0.00%
3.058	0.170	0.2140	0.04396	22.74	2.058	0.05165	0.162	4.52%
3.988	0.135	0.1546	0.01957	51.10	2.988	0.02136	0.133	1.33%
5.878	0.0860	0.09612	0.01012	98.82	4.878	0.006694	0.0894	3.98%
8.044	0.0620	0.06546	0.003459	289.1	7.044	0.002805	0.0627	1.06%
10.75	0.0450	0.04589	0.0008936	1119	9.75	0.001299	0.0446	0.90%

Table 8: Process for determining $\bar{\sigma}'_f$ for 7075–T6, illustrating error correction effectiveness.

k_t	σ'^{*}_f	σ'^{i}_f	δ	$1/\delta$	(k_t - 1)	σ'^{δ}_f	$\bar{\sigma}'^{i}_f$	% error
1.000	0.841	0.841	0		0.000		0.841	0.00%
3.058	0.170	0.2140	0.04396	22.74	2.058	0.05165	0.162	4.52%
3.988	0.135	0.1546	0.01957	51.10	2.988	0.02136	0.133	1.33%
5.878	0.0860	0.09612	0.01012	98.82	4.878	0.006694	0.0894	3.98%
8.044	0.0620	0.06546	0.003459	289.1	7.044	0.002805	0.0627	1.06%
10.75	0.0450	0.04589	0.0008936	1119	9.75	0.001299	0.0446	0.90%

Table 9: Process for determining $\bar{\varepsilon}'_f$ for 7075–T6, illustrating error correction effectiveness.

k_t	ε'^{*}_f	ε'^{i}_f	δ	$1/\delta$	(k_t - 1)	ε'^{δ}_f	$\bar{\varepsilon}'^{i}_f$	% error
1.000	0.841	0.841	0		0.000		0.841	0.00%
3.058	0.170	0.2140	0.04396	22.74	2.058	0.05165	0.162	4.52%
3.988	0.135	0.1546	0.01957	51.10	2.988	0.02136	0.133	1.33%
5.878	0.0860	0.09612	0.01012	98.82	4.878	0.006694	0.0894	3.98%
8.044	0.0620	0.06546	0.003459	289.1	7.044	0.002805	0.0627	1.06%
10.75	0.0450	0.04589	0.0008936	1119	9.75	0.001299	0.0446	0.90%

Table 10: Process for determining $\bar{\sigma}'_f$ for 4340, illustrating error correction effectiveness.

k_t	σ'^{*}_f	σ'^{i}_f	δ	$1/\delta$	(k_t - 1)	σ'^{δ}_f	$\bar{\sigma}'^{i}_f$	% error
1.000	0.841	0.841	0		0.000		0.841	0.00%
3.058	0.170	0.2140	0.04396	22.74	2.058	0.05165	0.162	4.52%
3.988	0.135	0.1546	0.01957	51.10	2.988	0.02136	0.133	1.33%
5.878	0.0860	0.09612	0.01012	98.82	4.878	0.006694	0.0894	3.98%
8.044	0.0620	0.06546	0.003459	289.1	7.044	0.002805	0.0627	1.06%
10.75	0.0450	0.04589	0.0008936	1119	9.75	0.001299	0.0446	0.90%

Table 11: Process for determining $\bar{\varepsilon}'_f$ for 4340, illustrating error correction effectiveness.

k_t	ε'^{*}_f	ε'^{i}_f	δ	$1/\delta$	(k_t - 1)	ε'^{δ}_f	$\bar{\varepsilon}'^{i}_f$	% error
1.000	0.841	0.841	0		0.000		0.841	0.00%
3.058	0.170	0.2140	0.04396	22.74	2.058	0.05165	0.162	4.52%
3.988	0.135	0.1546	0.01957	51.10	2.988	0.02136	0.133	1.33%
5.878	0.0860	0.09612	0.01012	98.82	4.878	0.006694	0.0894	3.98%
8.044	0.0620	0.06546	0.003459	289.1	7.044	0.002805	0.0627	1.06%
10.75	0.0450	0.04589	0.0008936	1119	9.75	0.001299	0.0446	0.90%

B Regression Data

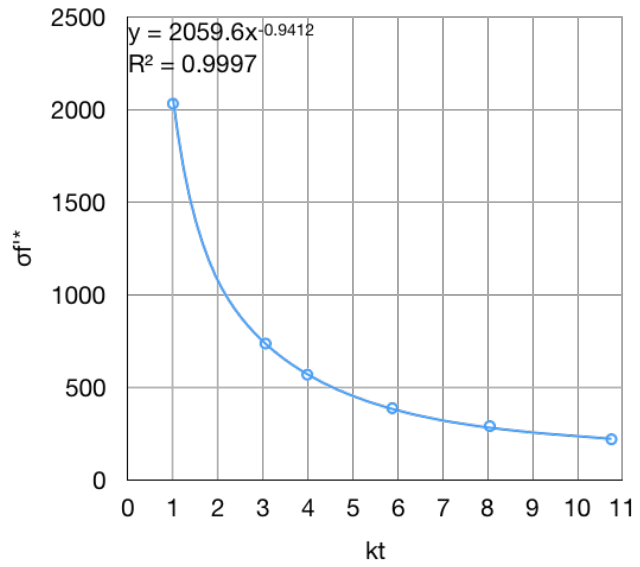

Figure 37: Trends of $\sigma_f'^*$ for Ti6Al4V (power law regression).

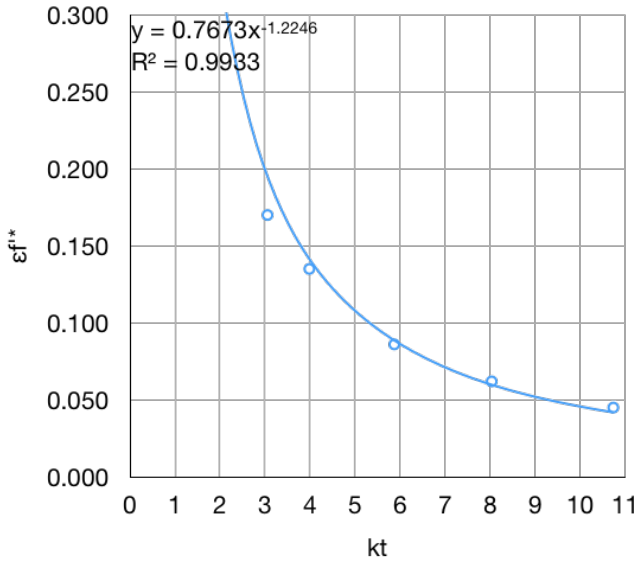

Figure 38: Trends of $\varepsilon_f'^*$ for Ti6Al4V (power law regression).

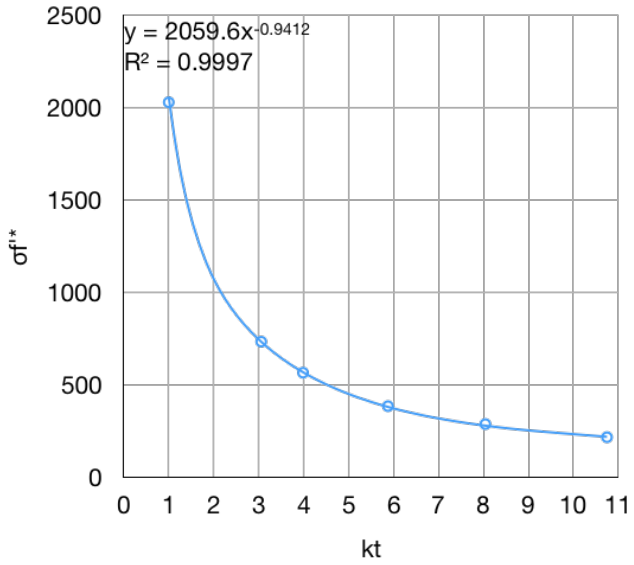

Figure 39: Trends of $\sigma_f'^*$ for 7075–T6 (power law regression).

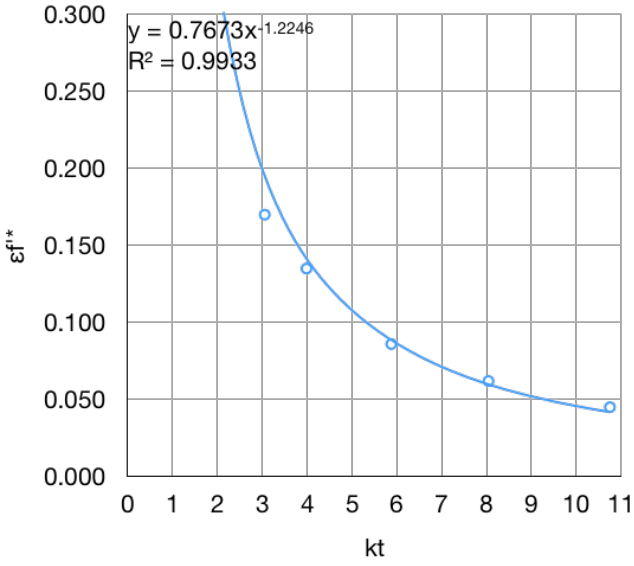

Figure 40: Trends of $\varepsilon_f'^*$ for 7075–T6 (power law regression).

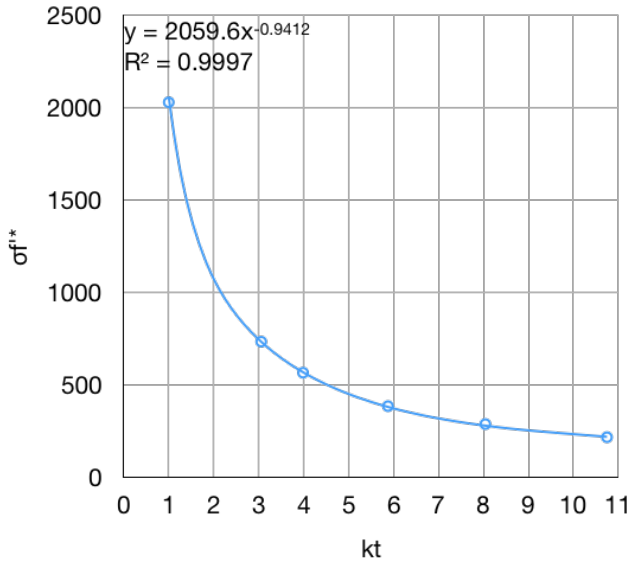

Figure 41: Trends of $\sigma_f'^*$ for 4340 (power law regression).

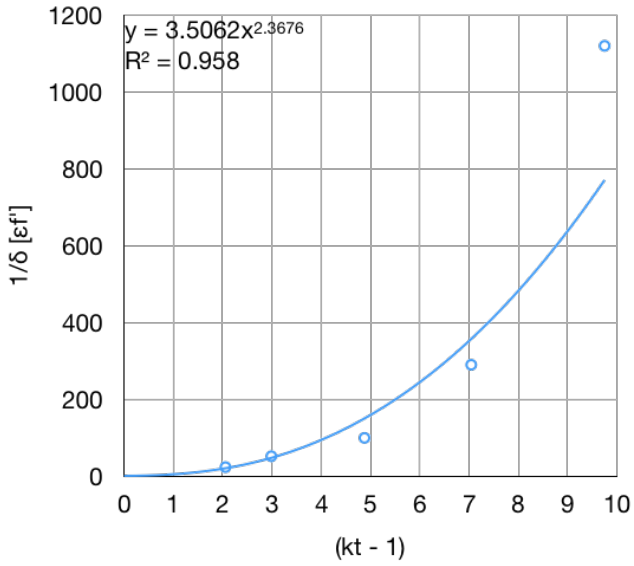

Figure 42: Trends of $\varepsilon_f'^*$ for 4340 (power law regression).

C Correction Factor

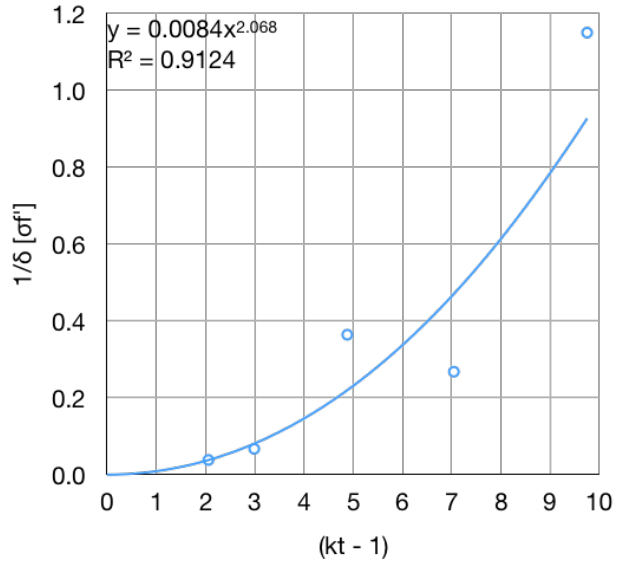

Figure 43: Inverse of correction factor of $\sigma_f'^*$ for Ti6Al4V (power law regression), computing parameters f and g.

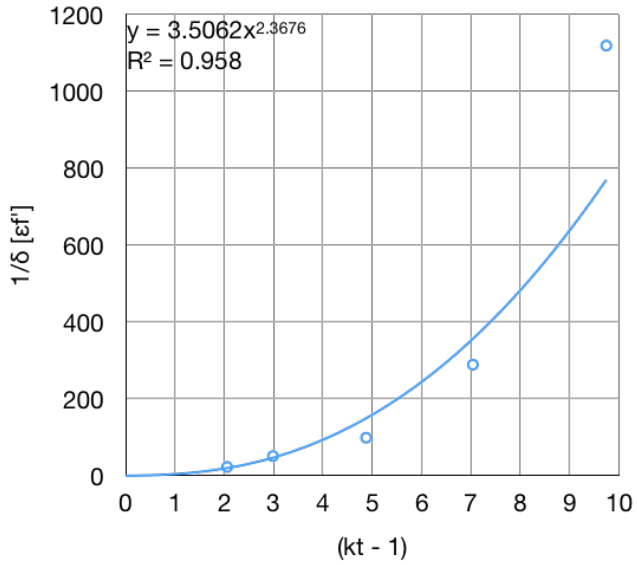

Figure 44: Inverse of correction factor of $\varepsilon_f'^*$ for Ti6Al4V (power law regression), computing parameters m and p.

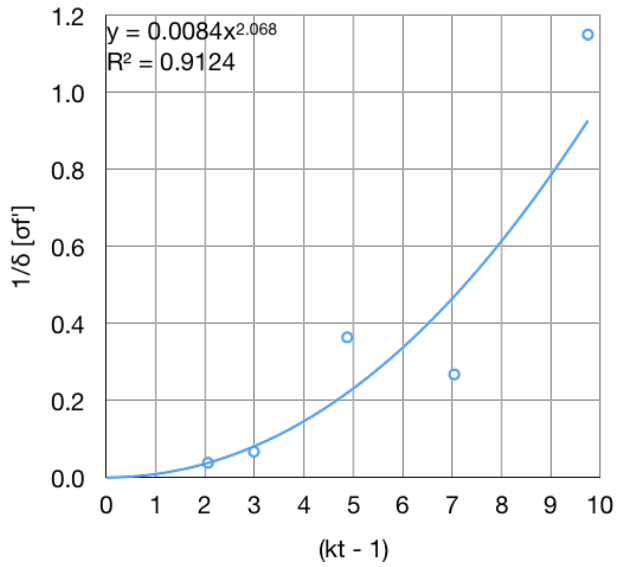

Figure 45: Inverse of correction factor of $\sigma_f'^*$ for 7075–T6 (power law regression), computing parameters f and g.

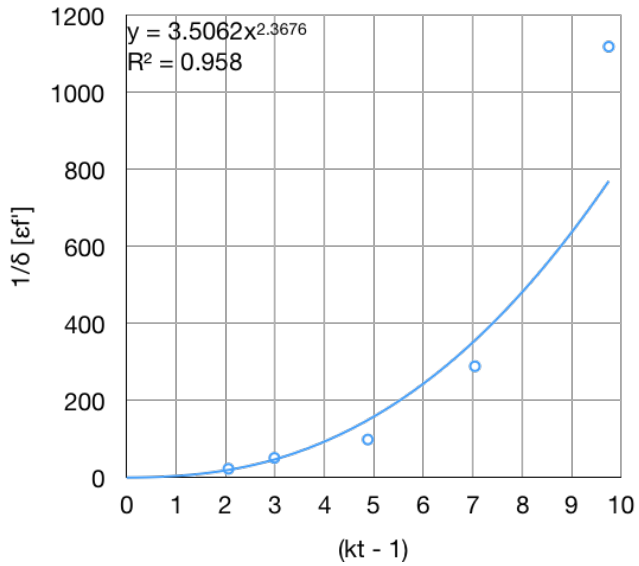

Figure 46: Inverse of correction factor of $\varepsilon_f'^*$ for 7075–T6 (power law regression), computing parameters m and p.

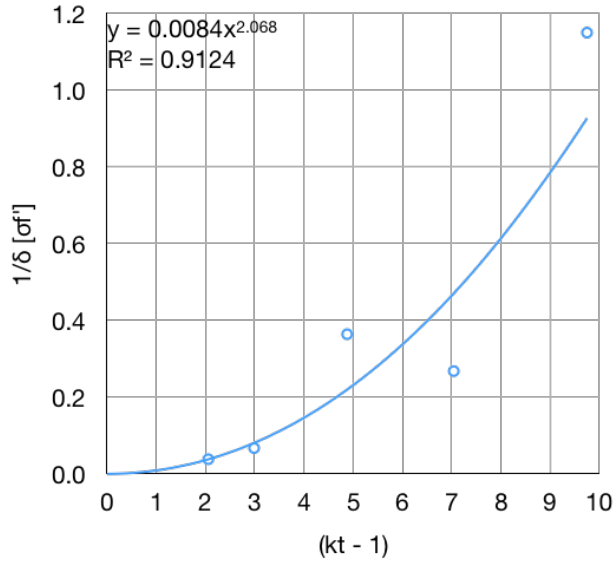

Figure 47: Inverse of correction factor of $\sigma_f'^*$ for 4340 (power law regression), computing parameters f and g.

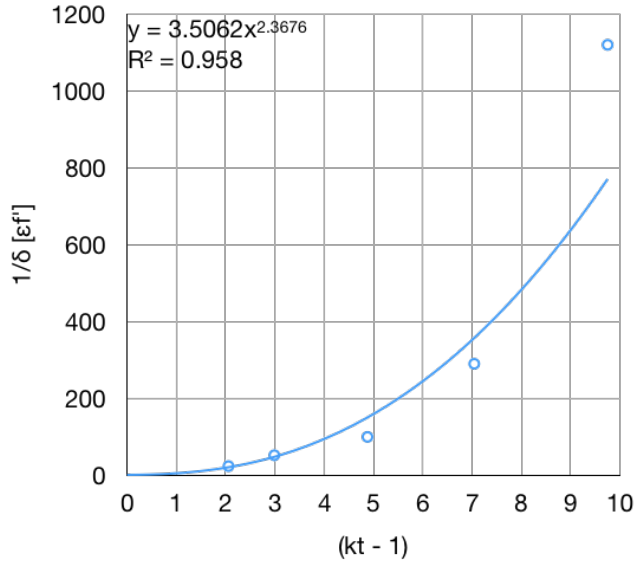

Figure 48: Inverse of correction factor of $\varepsilon_f'^*$ for 4340 (power law regression), computing parameters m and p.

D S–N Comparison With Model

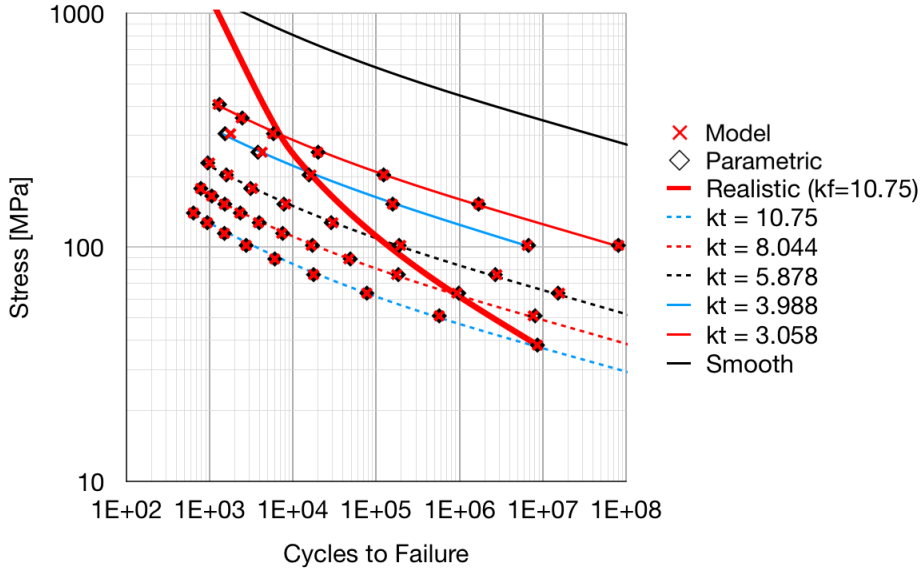

Figure 49: S–N comparison between smooth FEA simulation, notched FEA simulation, smooth with parametrically determined $\sigma_f'^*$ and $\varepsilon_f'^*$, smooth with computed $\bar{\sigma}_f'$ and $\bar{\varepsilon}_f'$ (Model), and a realistic k_f representation for Ti6Al4V.

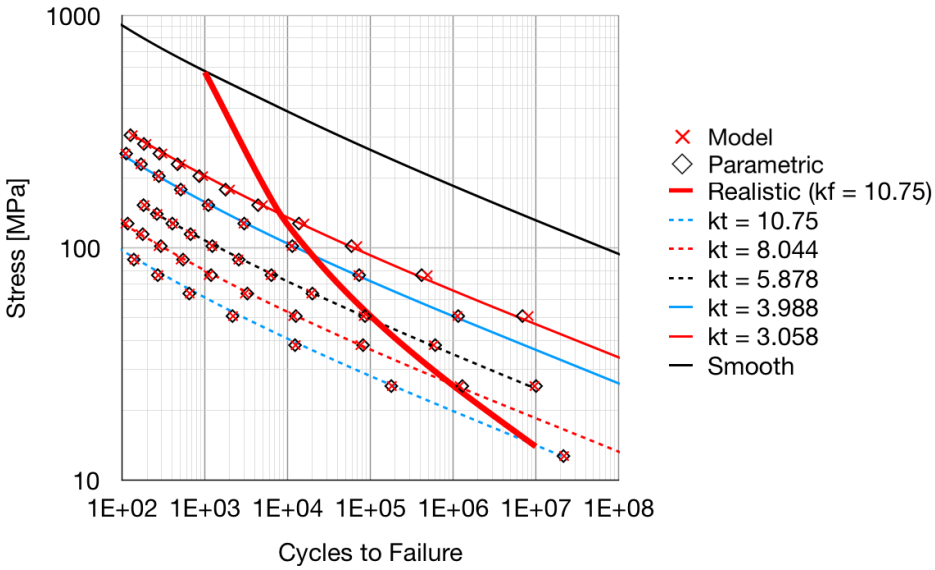

Figure 50: S–N comparison between smooth FEA simulation, notched FEA simulation, smooth with parametrically determined $\sigma_f'^*$ and $\varepsilon_f'^*$, smooth with computed $\bar{\sigma}_f'$ and $\bar{\varepsilon}_f'$ (Model), and a realistic k_f representation for 7075–T6.

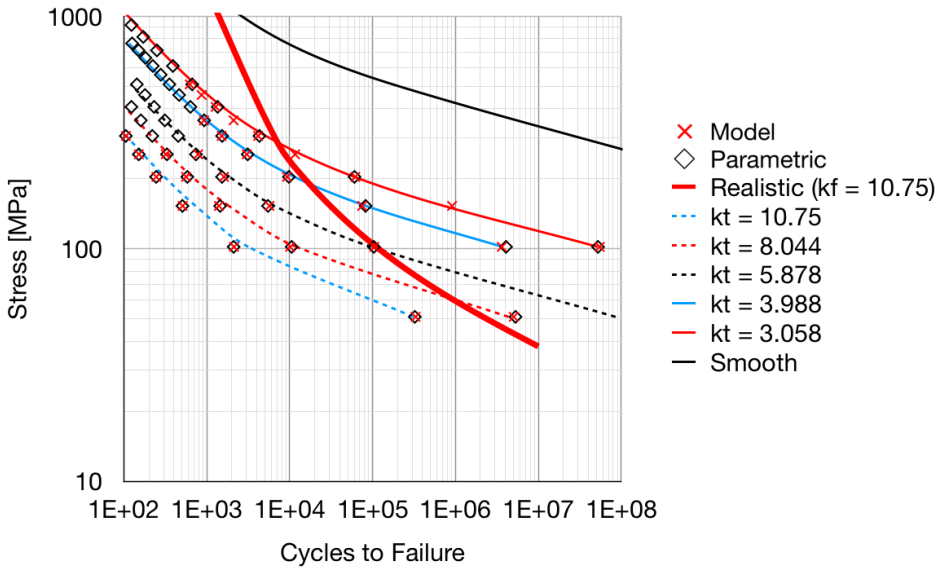

Figure 51: S–N comparison between smooth FEA simulation, notched FEA simulation, smooth with parametrically determined $\sigma_f'^*$ and $\varepsilon_f'^*$, smooth with computed $\bar{\sigma}_f'$ and $\bar{\varepsilon}_f'$ (Model), and a realistic k_f representation for 4340.